CHARACTERIZING MESO-MECHANICAL PROPERTIES OF ULTRA-THIN PLAIN WOVEN FIBRE COMPOSITES UNDER LARGE DEFORMATIONS

Weerasinghe W. U. D

228064H

Master's in Civil Engineering (Major component by Research)

Department of Civil Engineering
Faculty of Engineering

University of Moratuwa
Sri Lanka

May 2025

CHARACTERIZING MESO-MECHANICAL PROPERTIES OF ULTRA-THIN PLAIN WOVEN FIBRE COMPOSITES UNDER LARGE DEFORMATIONS

Weerasinghe W. U. D

228064H

Dissertation submitted in partial fulfillment of the requirements for the degree
Master’s in Civil Engineering (Major component by Research)

Department of Civil Engineering
Faculty of Engineering

University of Moratuwa
Sri Lanka

May 2025

DECLARATION

I declare that this is my own work and this Dissertation does not incorporate without acknowledgement any material previously submitted for a Degree or Diploma in any other University or Institute of higher learning and to the best of my knowledge and belief it does not contain any material previously published or written by another person except where the acknowledgement is made in the text. I retain the right to use this content in whole or part in future works (such as articles or books).

Signature: Date: 13/05/2025

The supervisors should certify the Dissertation with the following declaration.

The above candidate has carried out research for the Master's in Civil Engineering (Major component by Research) Dissertation under our supervision. We confirm that the declaration made above by the student is true and correct.

Name of Supervisor: Prof. Chinthaka Mallikarachchi

Signature of the Supervisor: Date: 14/05/2025

Name of Supervisor: Dr. Sumudu Herath

Signature of the Supervisor: Date: 14/05/2025

DEDICATION

This thesis is dedicated to my family, whose unwavering support, love, and encouragement have been my greatest source of strength throughout this journey. To my parents, who have instilled in me the values of hard work, perseverance, and curiosity, and who have always believed in my dreams. To my mentors and professors, whose guidance and knowledge have been invaluable, helping me shape my path in the field of engineering. Finally, to my friends and colleagues, who have shared this journey with me, providing support and camaraderie. This work is a testament to all of you, whose belief in me made this accomplishment possible. Thank you for being part of this journey.

ACKNOWLEDGEMENT

First and foremost, I would like to express my deepest gratitude to my supervisors, Prof. Chinthaka Mallikarachchi and Dr. Sumudu Herath, whose guidance, support, and mentorship have been invaluable throughout this research. Their expertise, encouragement, and constructive feedback have played a pivotal role in the successful completion of this work.

Also, I am grateful to the progress review and final evaluation committee for their valuable comments and support throughout the research.

Special thanks to the Deployable structures research group for giving me motivation and guidance throughout the research.

I am also grateful to the faculty and staff at the Department of Civil Engineering, University of Moratuwa, for providing a stimulating and supportive environment that has nurtured my academic and professional growth. Special thanks to my colleagues and friends for their camaraderie, insightful discussions, and encouragement during challenging moments.

I am profoundly appreciative of the support provided by my family, whose belief in my abilities has been my greatest motivation. Their unwavering support and encouragement have been a constant source of strength.

This research would not have been possible without the financial support of the National Research Council, provided through grant no. 2020-080. I am sincerely thankful for this funding, which has been essential in enabling the resources and facilities necessary to undertake this study.

Finally, to everyone who has contributed to this journey in ways big and small, I offer my heartfelt thanks. This accomplishment is a testament to your support and belief in my work.

Thank you all.

ABSTRACT

Ultra-thin woven fibre composite structures offer high strength-to-weight ratios and flexibility, making them highly used for aerospace and other applications requiring lightweight, durable materials. However, understanding and predicting the mechanical behaviour of these composites under large deformations, particularly their flexural response and bending stiffness, remains a challenge. This study presents a comprehensive investigation into the meso-mechanical properties of ultra-thin plain woven composites under conditions of extreme curvature. Using finite element modelling, this research focuses on accurately capturing the bending behaviour and assessing the impact of inter-tow slipping and material non-linearity, which are pivotal in understanding the reduction in bending stiffness observed at high curvatures.

A detailed numerical model based on a Representative Unit Cell approach was developed in Abaqus software, incorporating Periodic Boundary Conditions to reflect the composites meso-structural attributes. To simulate realistic conditions, both geometrical and material non-linearities were introduced. This approach enabled a robust analysis of cohesive interactions between fibre tows and the resin matrix, which are crucial for replicating the observed reduction in bending stiffness at higher curvatures. The FE model was calibrated and validated against experimental results from the literature, showing strong agreement with empirical data and confirming the model's predictive capabilities.

Results indicate that interfacial interactions, coupled with material non-linearity, play significant roles in the mechanical response of these composites, particularly under large bending strains. The study successfully captures these phenomena, providing a framework for further parametric studies and highlighting the necessity of mesoscale modelling for such complex materials. The findings offer valuable insights for optimizing the design of ultra-thin woven composites for use in deployable aerospace structures and other applications, contributing to the development of more efficient and reliable structural components.

Keywords: Thin woven composites, Meso-mechanical modeling, tow non-linearity, Inter-tow slipping

TABLE OF CONTENTS

CHAPTER 1

INTRODUCTION

1.1 Overview

Ultra-thin plain woven fibre composite structures have increasingly become a focus of attention across aerospace, automotive, and manufacturing industries due to their unique combination of high strength-to-weight ratios, damage tolerance, and versatile mechanical properties. These composites, characterised by interwoven fibre architecture, allow for tailored mechanical properties that are highly desirable in applications where both durability and lightweight construction are paramount.

In particular, Lightweight deployable composite structures have emerged as an appealing replacement for conventional aerospace structures as the those applications demand higher storage efficiency. The payload and stowage capacity of launch vehicles restrict the construction of large space structures such as solar sails and reflector antennas. Most space structures, however, have far greater dimensions than the launchers. The concept of deployable structures, on the other hand, enables a large structure to pack into a compact form for stowage and transportation and then extend back to the operational configuration. Ultra-thin woven composites are becoming popular in use for deployable structures because of their favourable material properties. The Antenna for the Mars Express Sub-Surface Sounding Radar Altimeter (MARSIS) sounding radar, which was 40 m long and folded as illustrated in Figure 1.1, was a primeval application of these self-deployable structures in aerospace industry [1].

For ultra thin woven composites to be successfully used and optimised in future structures, accurate material behaviour and failure mechanism predictions are crucial. Predictive models of ultra thin woven fibre composite are more complicated and have a higher degree of approximation due to the complexity of the structure and the existence of hierarchy and scale levels. Additionally, these models subjects to a high degrees of uncertainty in the projections caused by errors that keep piling up as the hierarchical levels are advanced [2].

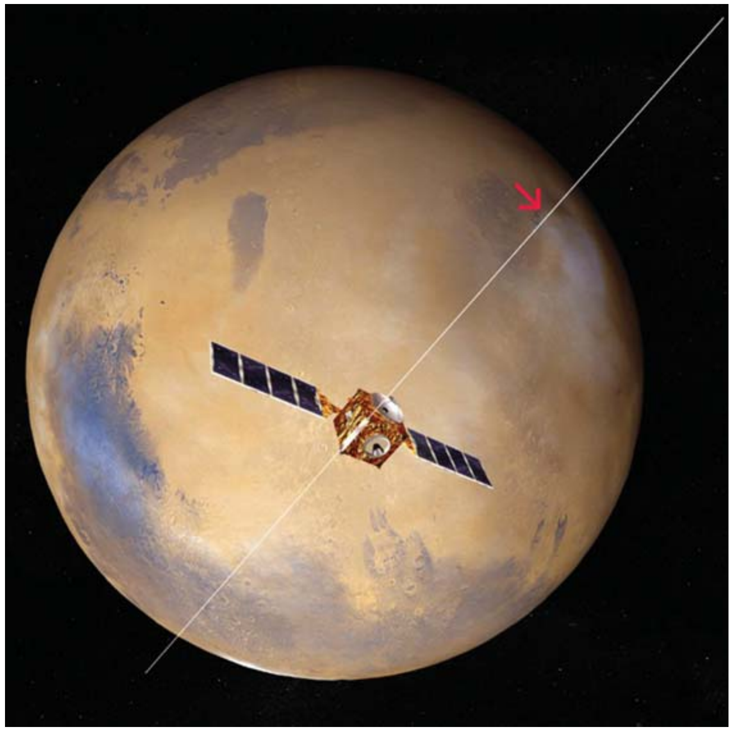

Fig. 1.1: MARSIS boom (source: ESA)

1.2 Challenges

Deployable structures, such as those used in aerospace applications, experience significant deformations during folding and deployment, making it essential to accurately predict the mechanical properties of woven fibre composites under high curvature. Reliable mechanical property predictions enable effective optimization and thorough pre-use studies, reducing the risk of in-service failures. A notable example highlighting this need is the initial failure of the MARSIS spacecraft to fully deploy upon reaching Mars orbit. This failure could potentially have been avoided with a better understanding and accurate prediction of the mechanical properties of the composite materials used, underscoring the importance of precise material characterization in such critical applications.

The deployable mechanisms of space structures are characterized by their technical complexity, challenging operational modes, exposure to harsh space environments, and strict resource limitations. This requires extensive physical testing during development, a process that is not only time consuming but also costly to simulate and assess extreme environmental conditions [3]. Numerical modelling plays a crucial role in reducing both development time and costs by enabling the effective simulation of complex materials, such as woven fibre composites, commonly used in aerospace structures. However, an efficient and practical computational methodology for accurately characterizing these woven composite structures under large deformations remains undeveloped. The primary challenges are the high geometric complexity and intricate mechanical behaviour of these materials, particularly for large deployable structures, which demand both accuracy and computational efficiency to capture the critical geometric architecture within reasonable costs.

Conducting virtual numerical simulations is essential to optimize future structures, maximize efficiency, reduce testing costs, and minimize risks. Advanced simulation tools can enhance design, improve testing value, and significantly reduce the required scale and frequency of physical tests. Thus, developing robust finite element analysis methods for both linear and non-linear simulations is crucial.

1.3 Scope and aim

The primary objective of this research is to develop a meso-mechanical finite element (FE) model capable of accurately representing the bending behaviour of ultra-thin plain woven composite laminates under the conditions of extreme curvatures.

Literature reveals a significant reduction in the bending stiffness of these ultra-thin structures when subjected to higher curvatures, as demonstrated by physical experiments. Mallikarachchi and Pellegrino [4] observed an average reduction in bending stiffness of 33% with respect to the initial bending stiffness when specimens are subjected to the failure curvature of 0.203 mm^{-1}. They have carried out a series of tests using four-point bending test and platen folding test, respectively, to assess initial bending stiffness and failure point. These observations were further supported by the findings from a study undertaken by Ajay et. al [5] using column bending test followed by a theoretical calculations using geometry based method. Most recent study conducted by Gamage et al., [6] also confirmed the observed bending stiffness reduction at higher curvatures with a continuous plot of bending moment per unit length vs curvature for both linear and non-linear region obtained from column bending test.

Despite the extensive theoretical and numerical research conducted to capture the observed reduction in bending stiffness, taking into account phenomena such as inter-tow slipping, the accurate representation of flexural behaviour remains unresolved [3, 7, 8].

In this study, numerical approach using finite element method will be used focusing a Representative Unit Cell(RUC) modelled with Periodic Boundary Conditions (PBC). ABD matrix will be extracted from a set of linear analysis through ABAQUS/Standard [9] and validated with experiment results from literature. Then the analysis is extended in geometrically non-linear region to observe the bending stiffness variation at higher curvatures. In addition to accurate representation of cohesive behaviour which was earlier hypothesized as the dominant driver of bending stiffness reduction, non-linear material behaviour of constituents will be taken into account in this study to predict flexural behaviour of the composite.

Findings of the research will be able to homogenize micro and meso scale used in macro scale of the woven composite. Also, it will facilitate for better understanding of the complex behaviour and aid in effective optimization of future structures.

1.4 Chapter Organisation

Following the introduction chapter, these five chapters are organised to systematically address the research on characterizing the meso-mechanical properties of ultra-thin plain woven composite structures under large deformations.

Chapter 2 reviews relevant studies on woven fibre composites, including their mechanical characteristics, applications, experimental findings, and multi-scale modelling approaches. Additionally, it addresses analytical and numerical methods previously used to model these materials.

Chapter 3 details the geometric, material, and interaction properties of the fibres and resin, which are used in the numerical models. This chapter includes the methods for estimating both linear and non-linear properties critical for accurately simulating the material behaviour of ultra-thin woven composites.

Chapter 4 describes the development of the FE model, focusing on the geometric modelling of the RUC and the use of PBC within the Abaqus software. This chapter also outlines the methods used to incorporate material non-linearity and interfacial interactions.

Chapter 5 presents the findings from the FE simulations, comparing them with experimental data to validate the model. It discusses the bending stiffness variations at high curvatures and examines the effectiveness of the meso-scale modelling approach in capturing the complex mechanical behaviour of the composites.

Chapter 6 summarises the key findings, contributions, and limitations of the research. This chapter also suggests potential future research directions, focusing on refining predictive models and extending the applications of ultra-thin woven composites in engineering.

CHAPTER 2

LITERATURE REVIEW

2.1 Woven fibre composites

In applications requiring structural capacity to withstand diverse loading conditions, textile fibre structures act as composite reinforcements, enhancing strength, stiffness, and hardness beyond those of the matrix alone, ultimately resulting in highly effective and reliable composites. The specific architecture of these fabrics, significantly influences their mechanical behaviour, with options ranging from woven types (plain, triaxial, and satin) to non-woven, knitted, and braided configurations [2]. For woven fibre composites, property estimation is typically performed following standardized test methods (e.g., ASTM standards), though modifications to testing geometries are often necessary to capture micro-scale behaviours. In-plane properties such as shear resistance, tensile stiffness, and durability are affected by weave type, fibre interactions, volume fractions, and the angle of the laminate phase. These composites generally exhibit lower through-thickness stiffness and impact resistance, but when the architecture is configured into monolithic forms like tape springs and booms, they can be adapted for applications demanding higher out-of-plane performance [10]. At the meso-scale, the primary reinforcement components are the warp (longitudinal tows) and weft (perpendicular tows), with the matrix binding them in an interwoven pattern to create a robust structure suited for high-performance engineering applications.

2.2 Applications of Ultra-Thin Woven fibre Composites

In recent years, there has been a growing interest in the development and application of ultra-thin woven composites, Specially in the aerospace and transportation industries owing to their exceptional mechanical properties and versatility. The unique combination of thinness, lightweight, and high strength exhibited by these materials has sparked significant research endeavours to explore their potential applications. Compared to ordinary materials, this type of composite materials offer non-corrosive properties, dimensional stability, good conform-ability and tailorability [11]. This section aims to

Fig. 2.1: Deployable mast that elements affixed by mechanical hinges

provide a comprehensive overview of the current state of knowledge regarding the application of ultra-thin woven composites. By examining the existing body of literature, we seek to highlight the advancements, challenges, and potential opportunities that lie within this exciting field, paving the way for future innovations and technological advancements.

The aerospace industry has emerged as a prominent sector where the application of ultra-thin woven composites has gained significant traction. The limited space available within aerospace launching vehicles posses a significant challenge when it comes to accommodating large structures. The lack of available space necessitates innovative approaches, including the development of compact and lightweight materials, folding or deployable structures, and intricate packing arrangements. Convention method of realizing large structures is to use rigid elements affixed by mechanical hinges (Figure 2.1). Astromesh reflector from Northrop Grumman is an exemplar. But mechanical hinges require actuation using motor or spring and hence tend to be heavy and complex [12]. Unlikely, woven composite structures such as deployable booms and tape spring hinges are capable of storing strain energy during folding and use that stored energy in self-deploying process eliminating the need for mechanical motors and actuators. Thus, use of woven fibre composites become popular in large space structures like large antenna reflectors, solar arrays and solar sails. [8]

2.2.1 Strain energy deployed booms

A variety of various organisations (NASA, DLR, etc.) have been utilising thin shell structures based on the strain energy deployed idea for upcoming missions. Deployable shell structures can be with either open or closed cross sections[12]. Those deployable booms can be categorised into four basic categories: Storable Tubular Extendable Membrane (STEM) booms, Tape Spring booms, Triangular Roll-able and Collapsible (TRAC) booms, and Collapsible Tubular Mast (CTM) booms.

One of the earliest tubular deployable booms to fly was Astro Aerospace's Storable Extensible Tubular Member (STEM), which dates back to 1962. The STEM boom is flattened when it is coiled on a drum and, when it is deployed, a motorised mechanism causes it to return to its round, undamaged shape. [13]

The simplest and most popular type of deployable booms are tape spring booms. They have a curved cross-section, thin walls, and are straight. MARSIS is the first deployable antenna that has been used to look at the many layers of material that make up Mars' surface, especially in search of water. It is a tabular structure constructed of two S-glass/Kevlar composite di-pole booms, each measuring 10 meters in length and 3.8 centimetres in diameter, and a mono-pole, measuring 7 meters in length and 2.0 centimetres in diameter. These tubes were folded into 1.5 m segments and slotted in a 1.7 m $\times$ 0.3 m $\times$ 0.2 m cradle as shown in Figure 2.2.

When folding, tubular booms with thin walls encounter extreme curvatures, which can create tremendous stress and potentially cause the structure to fail. Longer slotted holes added to tubular booms allow some components of the structure to function as self-locking tape spring hinges, allowing substantial deflections in both folding and deploying process.[14]

The National Aeronautics and Space Administration (NASA) created CTM booms in 1965 with the primary intention of using them as flexible conduits for reactor fluids. These booms feature a closed cross-section that is created by joining two half-shells with an omega shape such that one half-shell is linked with the other upside-down 2.3. The German Aerospace Center (DLR) started creating carbon fibre reinforced poly-

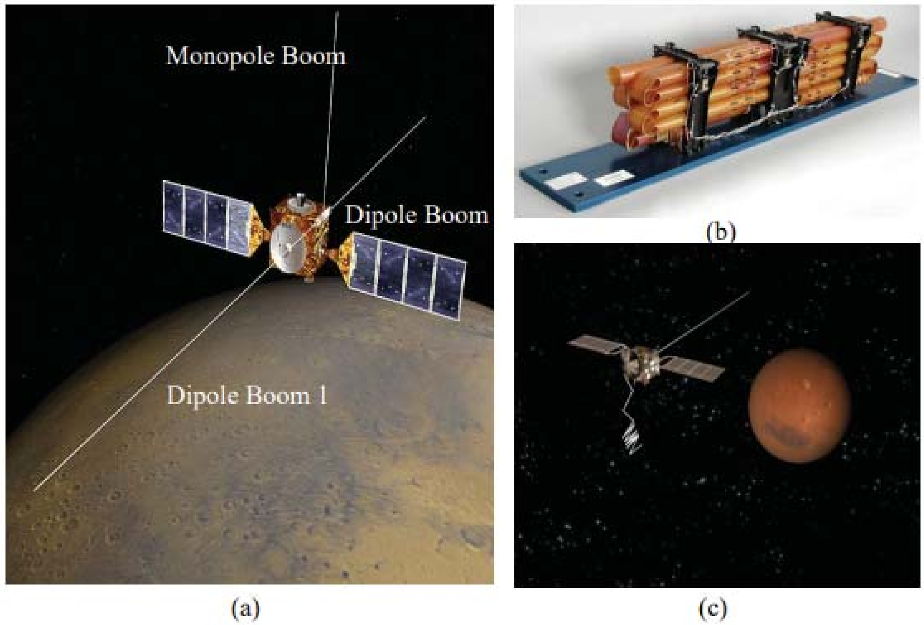

Fig. 2.2: MARSIS boom (a) Deployed configuration (b) Folded configuration (c) Deployment of second dipole boom (Courtesy: Astro Aerospace)

mer (CFRP) CTMs in a variety of scales in 1998 for various deployment mechanism designs[15].

Two tape springs, first created at the Air Force Research Laboratory, are joined along the same edge to make TRAC booms. Equal bending stiffness in both directions can be attained, which is an advantage over the tape spring, by altering design parameters. Since TRAC booms have an open cross-section, they can be flattened and wrapped more simply than CTMs[16].

2.3 Experimental Studies on woven composites

Experiments shed significant illumination on the mechanical performance, behaviour, and prospective applications of these structures. The purpose of this section is to investigate and evaluate the body of existing research on experimental studies done on ultra-thin woven composite structures. We aim to advance our understanding of these amazing materials by analysing and summarising the techniques, results, and limitations of these investigations.

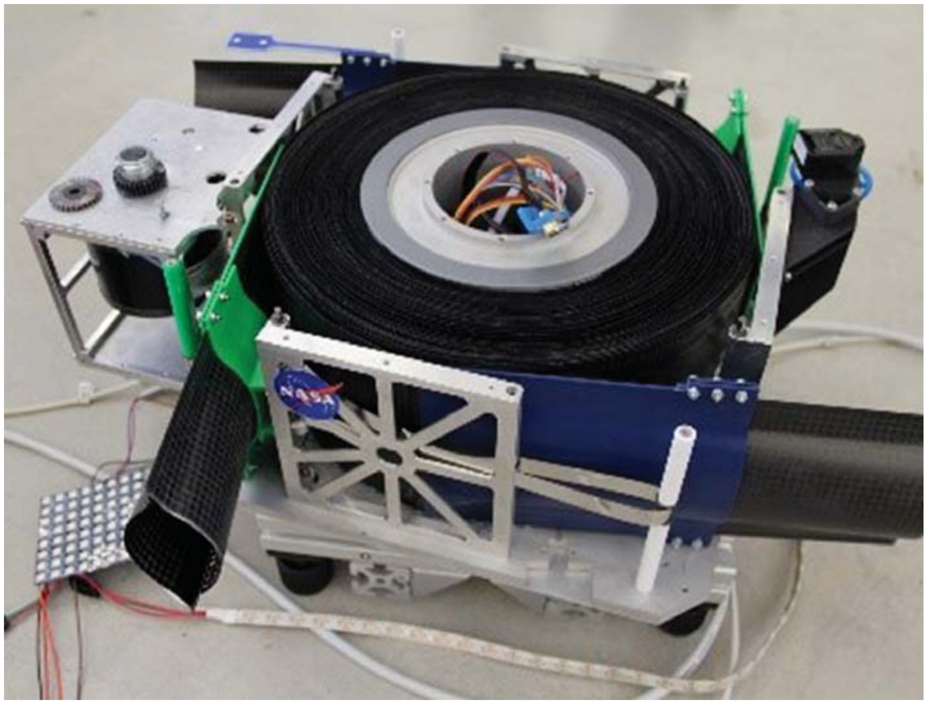

Fig. 2.3: Collapsible Tubular Mast (CTM) booms (Courtesy: Nasa.gov)

2.3.1 Non-linear flexural behaviour

On a two-ply T300-1k/Hexcel 913 plain weave laminate, Mallikarachchi [4] conducted a number of tests to determine the characteristics of ultra-thin woven fibre composites. Those were tensile tests, compression tests, shear tests, bending tests, twisting tests, and bi-axial tests. As their main focus is on aerospace applications, bending response is mainly investigated. Tensile response was also investigated in order to check the eligibility of the proposed finite element model. For the validation purpose of the finite element model, axial stiffness and shear stiffness is also investigated in this study.

To evaluate the bending response, four point bending test is performed instead of a three-point bending test since it generates more reliable and accurate observations at the region between two loading point as it is subjected to uniform bending moment. By taking into account the mean and standard deviation of 10 test results that took into account both loading and unloading, the initial bending stiffness was identified. According to the findings, the mean bending stiffness is 37.55 Nmm, with a 5.54 Nmm standard deviation.

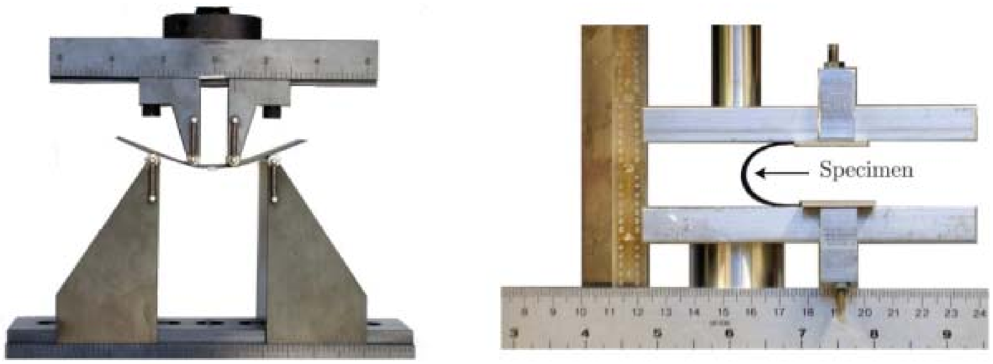

Fig. 2.4: (a) Four point bending test (b) Platen folding test [14]

Due to the wide elastic deformation range of thin laminates, four point bending test is not an acceptable option to obtain the failure point. As a result, the platen folding test was carried out by Mallikarachchi and Pellegrino [14], and the curvature at failure(κ_x) was determined by measuring the separation between the two platens(δ_1) in accordance with Equation (2.1). According to Sanford et al. [17], Equation (2.2), where P stands for force just prior to failure and b for sample width, can be used to compute the corresponding bending moment, M_x.

$$\kappa_x = \frac{2.3969}{\delta_1} \tag{2.1}$$

$$M_x = \frac{0.8346 P \delta_1}{b} \tag{2.2}$$

In this experiment, seven samples were taken into consideration. The failure moment was 5.068±0.293 Nmm/mm, and the failure occurred at a curvature of 0.203±0.01 mm^{-1}. The initial bending stiffness discovered by the four-point bending test, however, extrapolated, exhibits a substantially higher value of 7.623 Nmm/mm at failure curvature of 0.203mm^{-1}. Average stiffness reduction factor was calculated as 33% for the sample (Figure 2.5).

As a result, it is unattainable to optimise space structures using the initial linear predictions of stiffness.

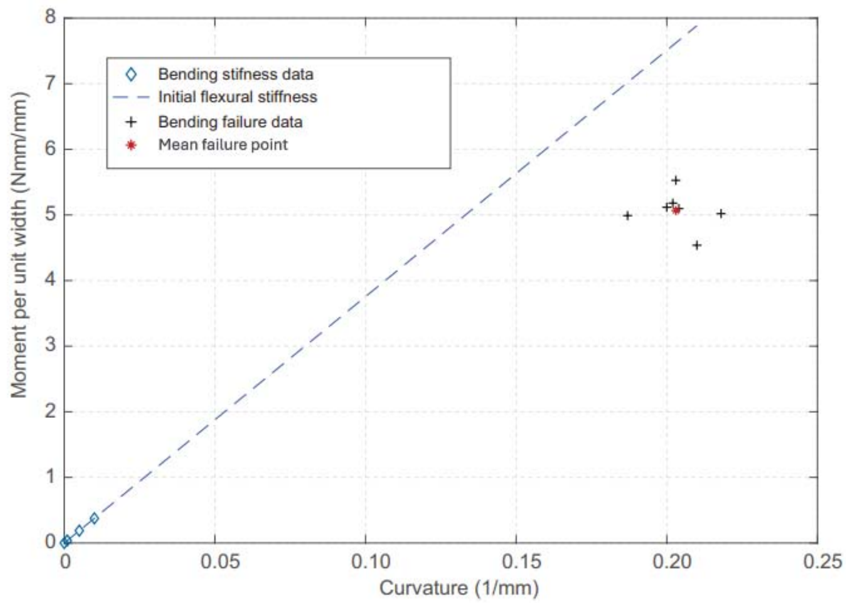

Fig. 2.5: Experimentally obtained moment-curvature response for ultra-thin woven fibre composites [14]

2.3.2 Column Bending Test

Despite the fact that the platen folding test reveals factual data on bending behaviour of ultra thin woven composites, there are some intrusions appended with it such as,

1. Moment distribution throughout the specimen is highly non-uniform in platen folding test leading large errors in processing of results

2. Pure moments are not acting at point of transition between flat and curved sections in platen folding test resulting in transverse loads that can induce impressive strains at coupon mid-section

Hence, as an alternative method, Fernandez and Murphy [18] recently came across with the column bending test to assess the bending behaviour of ultra thin woven composites to overcome those issues (Figure 2.6). In a different manner as the platen folding test, column bending test follows a geometric method to obtain bending behaviour in thin composite plates.

Following the method presented by Fernandez and Murphy [18], Ajay et. al.,[5] presented a preferable method for high strain composites to analyse the bending behaviour using a geometric based method adhering to following assumptions.

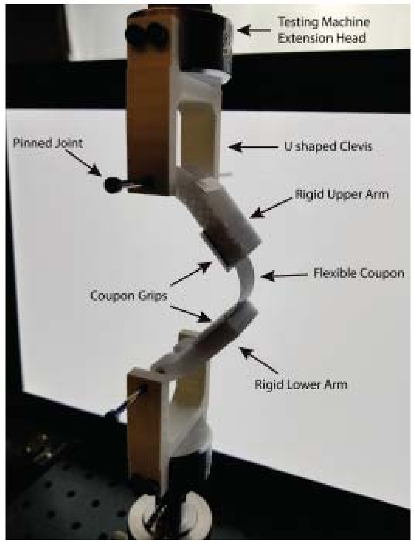

Fig. 2.6: Column Bending test experimental setup [5]

1. Neutral axis of the subjected plate always remains at the centre of the specimen during bending

2. Bending moment, and therefore the curvature, is close to constant along the arc length (If the coupon is sufficiently shorter compared to the length of the arms, the variation of the bending moment within the specimen is negligible)

3. Length of the specimen remains constant during the test, since the compressive loading is negligible compared to the bending moment

4. Specimen leaves the rigid arm at a perfect 90^0 angle

They calculated the maximum curvature calculated using a closed form solution derived geometrically (Figure 2.7) by assuming constant curvature through the specimen, with the prediction obtained analysing the test using Euler's elastica theory.

Equation 2.3 is proposed to calculate central angle ϕ of the bended specimen (Figure 2.7 using a transcendental method. Then the obtained central angle value can be used to calculate the subjected curvature (Equation 2.4). To calculate minimum and maximum moments at the instant, they have proposed simple geometric method given by equations 2.5 and 2.6 adhering to above stated assumptions. Equation 2.7 is proposed in the same study to calculate eccentricity of the maximum bending moment

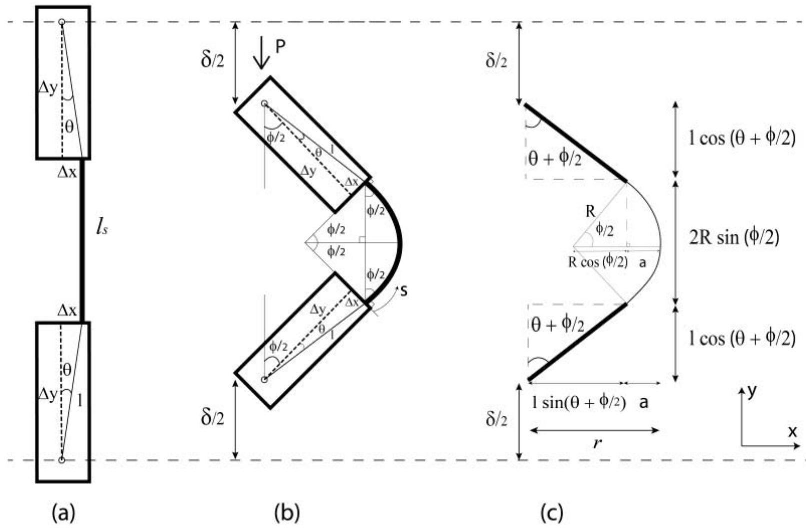

Fig. 2.7: Geometry of CBT (a) Initial geometry (b) Angles (c) Distances in test setup when a displacement δ is applied [5]

point from loading axis (r) which need to compensate the effects due to assumptions.

$$\frac{\delta_2}{l_s} = 1 - \frac{2}{\phi} sin\frac{\phi}{2} + 2\frac{l}{l_s}\left(cos\theta - cos\left(\theta + \frac{\phi}{2}\right)\right) \tag{2.3}$$

$$\kappa = \frac{\phi}{l_s} \tag{2.4}$$

$$M_{max} = P_1 r \tag{2.5}$$

$$M_{min} = P_1 l sin\left(\theta + \frac{\phi}{2}\right) \tag{2.6}$$

$$\frac{r}{s_1} = \frac{1}{\phi}\left(1 - cos\frac{\phi}{2}\right) + \frac{l}{s_1} sin\left(\theta + \frac{\phi}{2}\right) \tag{2.7}$$

Here, δ_2 is the total vertical displacement applied to loading arms along loading axis, l_s is the initial length of the sample, θ initial angular eccentricity of the sample from loading axis, κ curvature at the instance, M bending moment, P_1 is the applied load along the loading axis, l is the length of arms and s_1 is the curved length of the specimen.

Due to the assumptions, there were some effects to the calculated results such as effect of material non-linearity, effects of non-constant curvature through the specimen and effect of gravity due to weight unbalanced test configuration. In order to minimise those effect they have also proposed compensation methods listed below.

To incorporate the non-linear material behaviour to the calculations, they have imposed non-linear material properties only for fibres using equation and took neutral axis shifting phenomenon due to tension strengthening and compression softening into account when calculating bending stiffness for each curvature. Here, the shift in neutral plane was calculated solely utilising the equilibrium of internal forces through the thickness. Equation 2.8 , 2.9 and 2.10 presents the equations that they have used for the calculation of neutral axis position (y_{na}), Maximum bending moment(M_{max}) and bending stiffness (D_{11}) of the plate.

$$y_{na} = \frac{6 - \sqrt{36 - 3t^2\gamma^2\kappa^2}}{6\gamma\kappa} \tag{2.8}$$

$$M_{max} = \frac{1}{72}E_1\kappa t^3\sqrt{36 - 3t^2\gamma^2\kappa^2} \tag{2.9}$$

$$D_{11} = \frac{\partial M}{\partial \kappa} = \frac{E_1 t^3(6 - t^2\gamma^2\kappa^2)}{12\sqrt{36 - 3t^2\gamma^2\kappa^2}} \tag{2.10}$$

where γ is the degree of material non-linearity of tows, E_1 is the elastic modulus and t is the sample thickness. Here, when γ is increasing, deviation of the behaviour from linear is increasing

Despite the fact that they have obtained a linear relationship between normalised moment vs curvature for the simple geometric solution, after the above mentioned corrections for material non-linearity, they have observed that the normalised bending moment of the plate shows a geometrically non-linear behaviour against the applied curvature and the degree of geometrical non-linear behaviour tend to increase with the increasing material non-linearity of tows (Figure 2.8).

This also provided the evidence that the moment - curvature relationship is showing a geometrically non-linear behaviour in higher curvatures for ultra thin woven composites conforming the fact that it is unattainable to optimise space structures using the initial linear predictions of stiffness but the no-linear mechanical response.

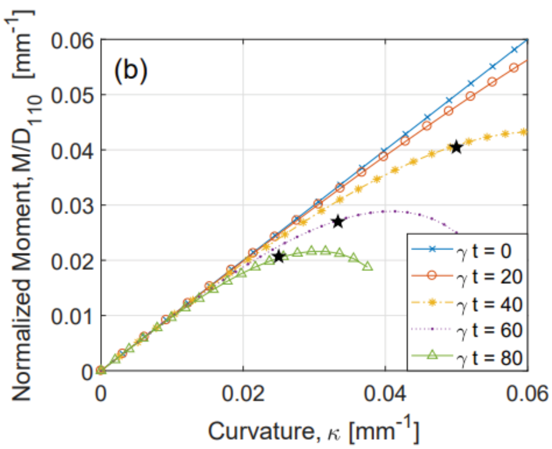

Fig. 2.8: Normalised Moment vs Curvature relationship for different degrees of material non-linearity of tows [5]

2.4 Multi-scale modelling

Complex geometry and non-linear behaviour of constituents hinder the prediction accuracy of mechanical behaviour of ultra-thin woven composites. There is a common practice popular among researchers involve three sequential modelling scales to combine the requirements of difference applications. Those scales can be defined based on the geometry and mechanical behaviour, and named as micro-scale, meso-scale and macro-scale. Multi scale modelling approach averts the higher computational cost that would be required by detailing at macro-scale and the excess information provided by the micro-scale. Higher accuracy and efficiency of the required information is obtained through merging different scales simultaneously.

Three main categories of multi-scale modelling approaches can be identified. Those are concurrent, hierarchical and hybrid methods. Hierarchical multi scale modelling approach is getting popular among researchers due to well defined scale transition and precise fundamentals on unique role of each scale. In this method, considered scales are associated in the same part of the domain and linking is achieved by volume averaging of field variables. Different scales of the boundary value problem are solved in parallel.

Applications of multi-scale modelling technique is diverse such as: composite

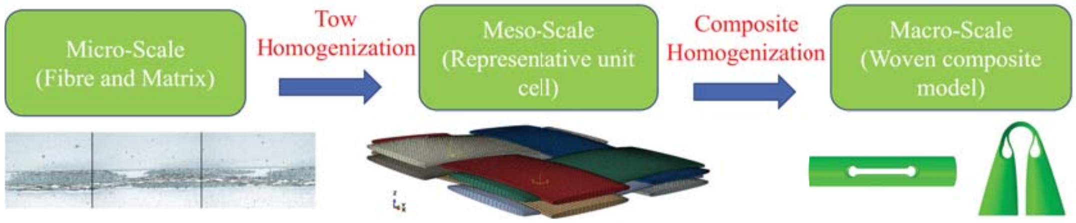

Fig. 2.9: Multi-scale modelling approach

structures [11], complex fluids[19], heat transfer[20], Conductivity[21], cardiac mechanics[22] and many more.

In this specific research we focus on aerospace engineering applications for thin woven composites.Solitary response of resin and fibre is examined on micro-mechanical scale allowing for their constitute properties and the composition. Mechanical behaviour of the composite is apprehended at the meso-scale considering a satisfactory representative volume of the continuum material. Geometric architecture and the interaction mechanism is assessed in this scale and usually constituents are modelled as homogeneous bodies. Overall response of the fabricated objects at complex deformations is examined at the macro-scale considering structure as a homogeneous mass (Figure 2.9).

Homogenisation techniques have been used in merging two sub sequential scales by considering appropriate properties and the satisfactory distribution assimilated from previous scale. Accurate coupling between each scales respecting mechanics and compatibility is at the cutting edge of multi-scale modelling.

2.5 Analytical Studies on Woven fibre composites

Considerable number of analytical studies have been conducted on woven fibre composites to investigate mechanical properties. Ishikawa and Chou [23] developed three different analytical models that depend on Classical Lamination Theory (CLT). While Mosaic model assumed iso-stress and iso strain fabrics and simulated cross-ply lami nates neglecting undulation [23]. Fibre undulation model took out-of-plain waviness of the yarns and calculated stiffness reduction due to yarn crimp. Mosaic model showed a good agreement with elastic properties while undulation model showed good results with low crimping woven fabrics. Above two models were bringing together to develop the bridge model.

Queck et al. [24] developed analytical method to characterise fabric mechanical behaviour using a unit cell representing continuum nature of the fabric. It was based on volume averaging formula which allowing calculation of average stiffness. Tsai et al. [25] presented a parallelogram spring model to inquire into the effect of architectonic factors such as volume fractions, braid angle etc. on mechanical behaviour.

Goyal [26], made inquiries about various architectonic parameters like stacking sequences and waviness ratio in 2×2 braids using CLT. Equivalent laminated materials with angle plies were modelled with a matrix layer in the middle. Then the results were compared with full 3-D FE model results and showed only a minor deviation.

2.5.1 Classical Lamination Theory

CLT is developed following the basics of Kirchhoff-Love hypothesis for shells. Here, each individual lamina is analysed for the relationship between in-plane stresses, in-plane strains and out-of-plane curvatures and integrated forces and moments through the thickness to form ABD matrix. It constitutes the relationship between static and kinematic variables. Here, kinematic variables are mid-plane strains and curvatures while static variables are in-plane force forces and out-of-plane moment resultants (Equation 2.11).

$$\left\{\begin{array}{c} N_x \\ N_y \\ N_{xy} \\ -- \\ M_x \\ M_y \\ M_{xy} \end{array}\right\} = \left(\begin{array}{ccccccc} A_{11} & A_{12} & A_{16} & | & B_{11} & B_{12} & B_{16} \\ A_{21} & A_{22} & A_{26} & | & B_{21} & B_{22} & B_{26} \\ A_{61} & A_{62} & A_{66} & | & B_{61} & B_{62} & B_{66} \\ -- & -- & -- & -- & -- & -- & -- \\ B_{11} & B_{21} & B_{61} & | & D_{11} & D_{12} & D_{16} \\ B_{12} & B_{22} & B_{62} & | & D_{21} & D_{22} & D_{26} \\ B_{16} & B_{26} & B_{66} & | & D_{61} & D_{62} & D_{66} \end{array}\right) \left\{\begin{array}{c} \varepsilon_x \\ \varepsilon_y \\ \gamma_{xy} \\ -- \\ \kappa_x \\ \kappa_y \\ \kappa_{xy} \end{array}\right\} \tag{2.11}$$

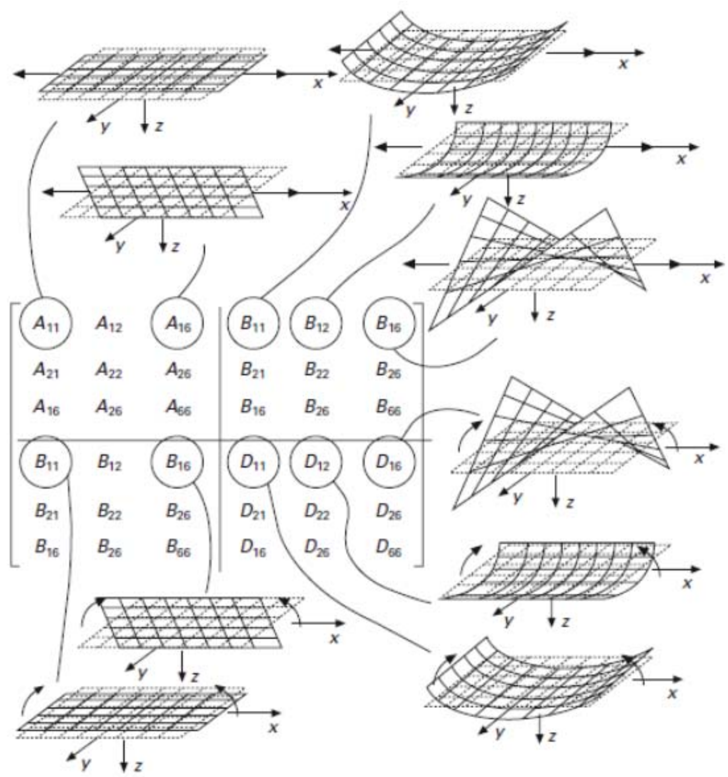

Fig. 2.10: Pictorial representation of deformed configurations corresponding to ABD matrix entities [7]

where, N denotes in plane force resultants, M denotes out of plane moment resultants and ϵ and κ denotes in plane strains and out of plane curvatures respectively. ABD matrix is consists with 3 sub matrices of A, B and D, each consisting with 9 elements. A matrix denotes the relationship of extensional parameters (in plane force resultants and strains). D matrix denotes the relation of bending parameters (out-of-plane moment resultants and curvatures) where B sub matrix denotes the coupling between bending and extension parameters. x and y denote the two principal directions of the laminate. Figure 2.10 gives a better explanation of deformed configuration corresponding to entities of ABD Stiffness matrix in a pictorial manner.

Due to symmetry, balanced orthotropic nature of plain-woven laminates, ABD matrix can be simplified with fewer unknown entries as given in Equation 2.12.

$$\begin{Bmatrix} N_x \\ N_y \\ N_{xy} \\ -- \\ M_x \\ M_y \\ M_{xy} \end{Bmatrix} = \begin{pmatrix} A_{11} & A_{12} & 0 & | & 0 & 0 & 0 \\ A_{21} & A_{22} & 0 & | & 0 & 0 & 0 \\ A_{61} & A_{62} & A_{66} & | & 0 & 0 & 0 \\ -- & -- & -- & -- & -- & -- & -- \\ 0 & 0 & 0 & | & D_{11} & D_{12} & 0 \\ 0 & 0 & 0 & | & D_{21} & D_{22} & 0 \\ 0 & 0 & 0 & | & 0 & 0 & D_{66} \end{pmatrix} \begin{Bmatrix} \varepsilon_x \\ \varepsilon_y \\ \gamma_{xy} \\ -- \\ \kappa_x \\ \kappa_y \\ \kappa_{xy} \end{Bmatrix} \tag{2.12}$$

CLT was originally designed to assess the behaviour of unidirectional composites. Lately it has been used to investigate the woven composites by idealising those as equivalent laminates that describe the woven architecture.

Due to complex woven architecture, some of the assumptions made while developing CLT are not valid such as middle section of the laminate presumed to be remain straightened and perpendicular to mid plane while it undergo bending. As described above, resultant forces and moments calculated by integrating through the thickness. That leads D matrix to be highly reliant on thickness of the laminate even though woven fibre composites are not constant in thickness due to interlacing nature of tows. Even though it predicts in-plane properties with a good accuracy, when it comes to bending properties it over-predicts by about 300% to 400% [3], [27].

2.6 Numerical Studies

Numerical studies are more favourable among researchers over physical experiments on ultra thin woven composited due to high cost associated with conducting experiments in their operating conditions. That is resulted from available techniques to adopt realistic architectural structure and material properties in advanced computational simulations. [8]

Finite element unit cell modelling can be identified as a major numerical technique used in estimating mechanical characteristics, obtaining 3-D strain fields and identifying failure mechanism of these composites [10]. Numerical models have been advantage over classical analytical techniques since they can synthesize realistic geometry of the composite using Computer Aided Drafting (CAD) tools. In addition FE models delineate stress stain distribution through the composite making it befitting to failure prediction [28].

Bigaud and Hamelin [29] developed a numerical method to predict both elastic properties and failure criteria along with a computer based program TIS3D. It allowed to models geometry of a textile with a polymer resin in a multi-scale manner. Properties at each scale were ascertained following energy methods and stress strain averaging [29]. Tan et al. (1997) developed a similar model to incorporate weaving types in the FE model and results showed a good agreement with theoretical data in geometrically linear region[30].

Taibei and Jiang [31] used commercially available Abaqus software package to examine the behavior of woven composites in the geometrically non-linear region. They used user defined subroutine to couple between different scales in the geometrically non-linear region.

Gasser [32] studied the behaviour of woven fibre composites using a dry fibre model instead of modeling the textile with overlaying resin. They simulated the endowment of the resin in mechanical behaviour using interaction methods.

Hivet et al, [33] examined the composite behaviour in geometrically non-linear region considering yarn crushing and concluded revealing the significance of both geometric changes and contact behaviour in predicting non-linear behaviour.

Ballhause et al, [34] developed a model based on Discrete Element Method(DEM) and performed dynamic analysis. Discrete mass units and rheological elements expounded the geometry and connections in the woven composite (Figure 2.11).

Bisse and Hivet [35] developed a FE representative unit volume with axial elements, considering the meso-level geometry. He assumed zero voids between tows and no penetrations of tows ensuring consistency (Figure 2.12).

Karkkainen and Sanker [36] developed a FE model in meso scale using homogenization theories based on Kirchhoff-Love theory for shells. Periodic boundary conditions were applied appropriately in that model to represent the continuum nature of the textile. As we described in analytical methods section, this model was able to constitute a relationship between kinematic and static variables in the form of ABD matrix

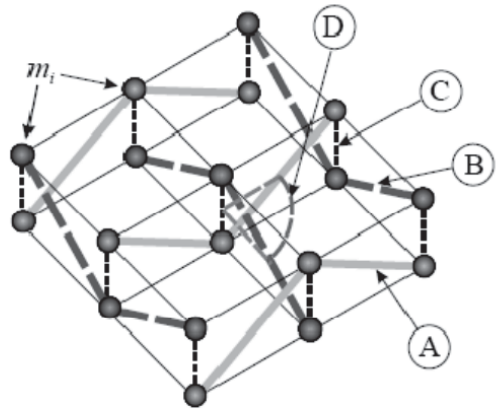

Fig. 2.11: Discrete Element Model (A; Warp, B:weft, C:Transverse yarn compression, D: rotational resistance, m: concentrated mass

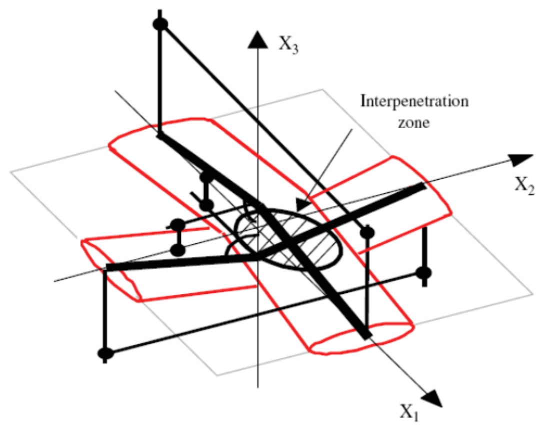

Fig. 2.12: Geometric idealization for axial element model [35]

(Figure 2.13).

Kueh and Pellegrino [37] characterized a Triaxial Weave Fabric (TWF) composite considering its 3D micro-structure after analytically predicting and validation of stiffness and failure parameters. They have adopted Kirchhoff plate theory in a finite element unit cell constructed with beam elements which follow Timashenko beam theory (Figure 2.14) in order to find the homogenised properties of the composite.

Mallikarachchi and Pellegrino [4] developed a more detailed unit cell for a two-ply plain woven composite considering various tow profiles such as rectangular and different roots of a sine wave (Figure 2.15). They investigated the behaviour of composite under small strains and revealed that despite the fact that beam models sufficiently pre-

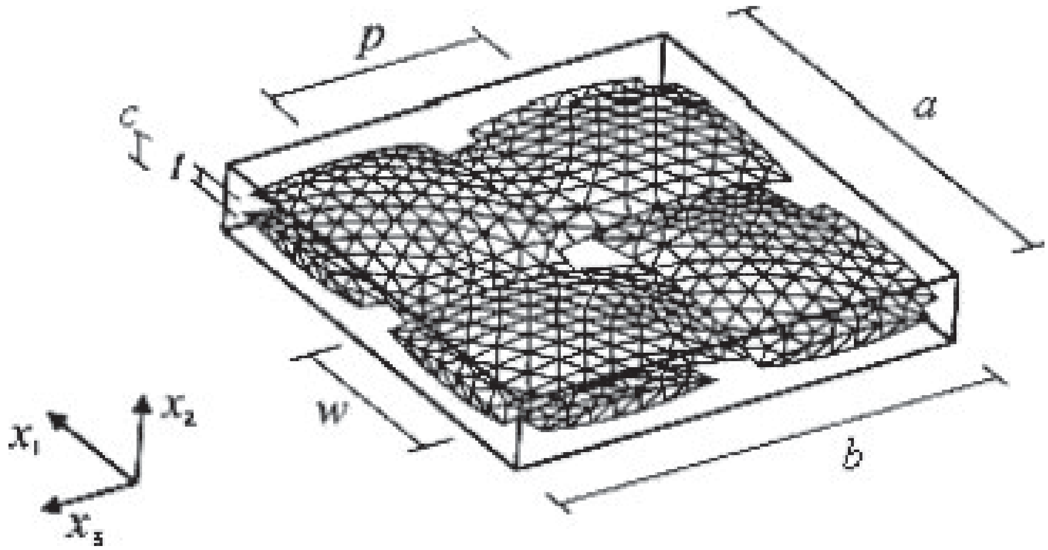

Fig. 2.13: RUC developped by Karkkainen and Sanker[27]

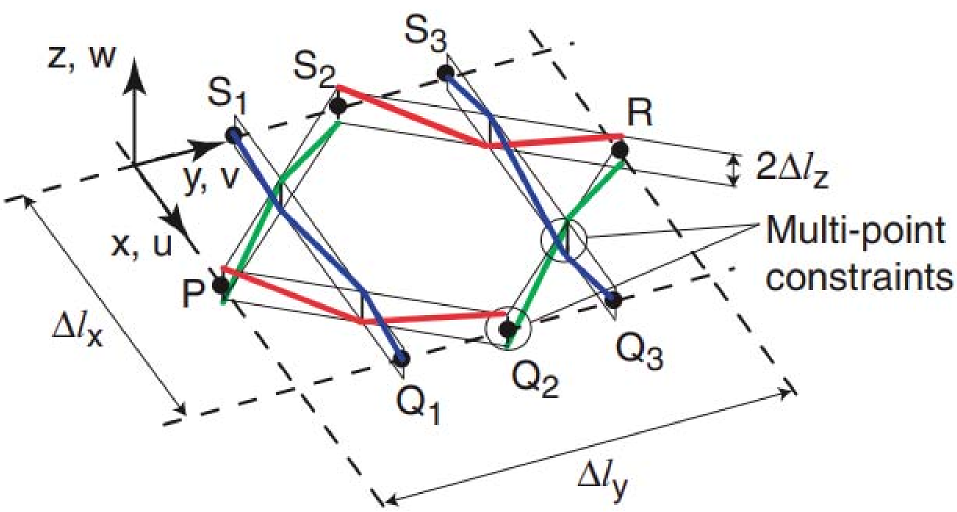

Fig. 2.14: Beam model by Kueh and Pellegrino[37]

dict bending stiffness, more realistic geometric representation is required in accurate prediction of in-plane properties.

Yapa and Mallikarchchi investigated the mechanical behaviour of ultra-thin woven fibre composites in higher strains by extending the Kirchhoff plate based analysis into geometrically non-linear region. Here, tow sections were idealised as equivalent

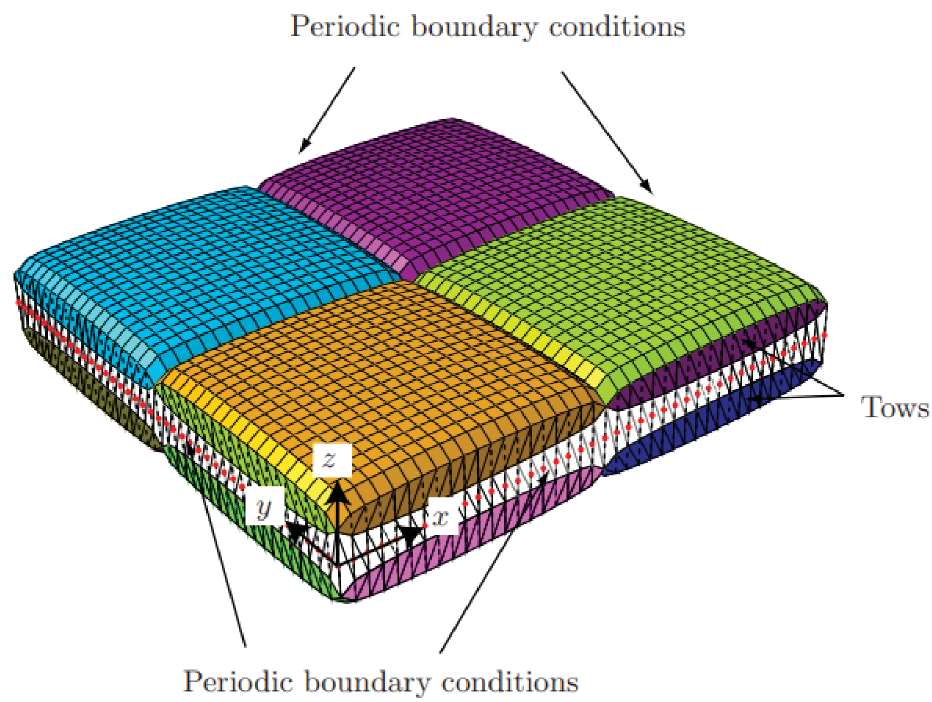

Fig. 2.15: Fourth root sine wave profile model by Mallikarachchi and Pellegrino (2011) [4]

rectangular cross sections and modelled using two-node linear beam elements. They revealed that the over constraining at interaction regions can cause non-convergence of solutions and both realistic geometry and accurate simulation of interaction properties significant in capturing the mechanical response of ultra-thin woven composites at high curvatures.

Wijesooriya et al., developed a RUC using shell elements to model tows and incorporated cohesive behaviour between interaction regions to simulate a more realistic representation with complying with the used computational cost. Also, they have incorporated both cohesive behaviour and damage at the interaction regions in a solid model and were able to capture a reduction in bending moment up to a curvature of 0.04 mm^{-1}. They concluded the study revealing accurate modelling of both cohesive behaviour and post failure behaviour is essential in capturing the accurate mechanical behaviour of thin woven composites [38].

Jayasekara et. al, developed a RUC following the same procedure but with more realistic geometry idealising equivalent tow geometry and waviness of cubic bezier spline (Figure 2.16. Tow geometry was developed using a commercially available TeX-GEN software package and imported into commercially available Abaqus software package for the simulations. That model was able capture the non-linear bending response up to a curvature value of 0.14 mm^{-1} [8].

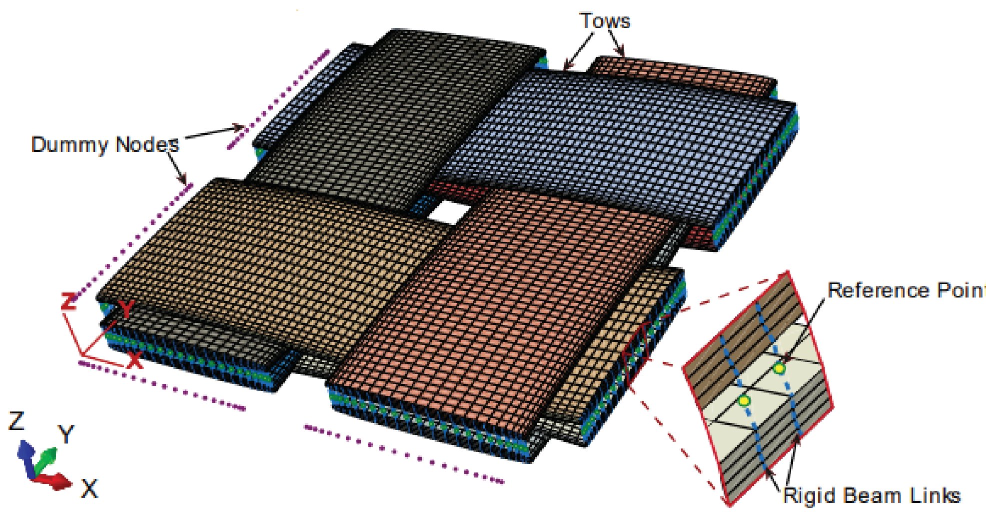

Fig. 2.16: RUC with Cubic Bezier spline wave profile [8]

Lomow et. al [39] used micro computed tomography images to construct the geometry of woven composites using VoxTex software package for the segmentation and Abaqus software package for mechanical simulations. Also, Green et al., developed a FE mesh with realistic geometry for woven fibre composites. That model was capable of accounting for minor deformations that tows can undergo during the fabricating process that can affect the overall performance of the composite (Figure 2.17).

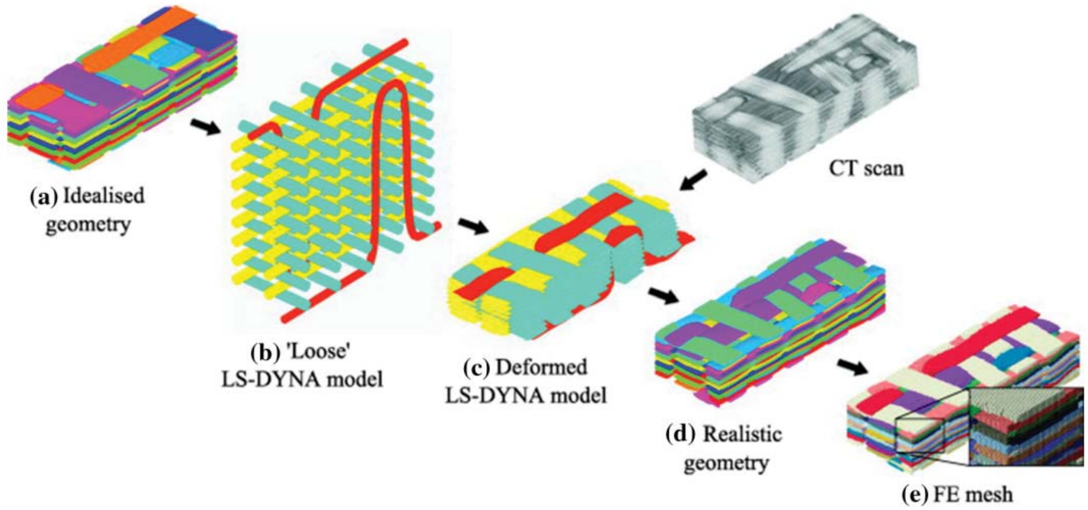

Fig. 2.17: Workflow process of CT scanned image based modelling [39]

CHAPTER 3

CONSTITUENT PROPERTIES

This chapter presents the constituent properties used in this study. Material properties used for constituents in both linear and non-linear regions, characteristic properties used in simulating different interactions, idealized geometric architecture of the composite and use of material orientation is discussed in this chapter. Fibre and resin properties in material non-linear region are obtained from manufacturer and the properties in material non-linear region is calculated based on literature. Interaction properties characterized considering resin behaviour in contact regions based on a past study and the geometric architecture is based on both measurements of the micro graphs and previous studies.

3.1 Geometric Properties

3.1.1 Tow geometry

3.1.1.1 Geometric parameters

Geometric parameters for tows are extracted from previous study by Mallikarachchi and Pallegrino. Tow cross sectional area(A), Weave length (ΔL) and tow thickness(a) were calculated using the micrographs (Figure 3.1) of the same composite specimens used in experimental studies considered in this study which is made of 1K/T300 carbon fibre and Hex-Ply 913 epoxy resin [4]. Average properties of ten cross sections from four specimens inferred from the study is presented in table 3.1.

Fig. 3.1: Micrograph of T300-1k/913 two ply plain weave laminate [4]

Weave length	2.664mm
Cross section area	0.0522 mm^2
Tow thickness	0.059mm

TABLE 3.1: Geometric parameters for tow [4]

3.1.1.2 Tow cross section and weave path

It is a common practice in studies of woven fibre composites to make use of idealized cross sections for property prediction [40]. There are a few software programs available for modelling textile composites geometrically. WiseTex and TexGen are two open access software packages that can be used to develops the geometry of tows from user inputs. While WiseTex computes tow geometry using energy minimisation algorithms, TexGen create the geometry using spline interpolation between user-defined node points [41], [42].

The tow cross section used in this investigation was a power elliptical shape defined by Equation 3.1 and 3.2 with a power of 0.5, as offered by the TexGen software. This shape has been shown in the literature [8, 43] to be well-suited and to correspond well with the micrograph of two-ply plain weave laminate.

$$C(t)_x = \frac{w}{2}cos(2\pi t) \qquad 0 \leq t \leq 1 \tag{3.1}$$

$$C(t)_y = \begin{cases} \frac{a}{2}(sin(2\pi t))^n & 0 \leq t \leq 0.5 \\ -\frac{a}{2}(-sin(2\pi t))^n & 0.5 \leq t \leq 1 \end{cases} \tag{3.2}$$

where, w width, n cross section power and a thickness.

Width of the tow was calculated in accordant with observed maximum tow thickness and cross section area listed in Table 3.1 using Equation 3.3 and acquired a value of 1.013 mm.

$$A = 0.278\pi hw \tag{3.3}$$

where, A cross section area, h maximum tow thickness and w tow width.

The cubic Bezier spline interpolation generated by the TexGen preprocessor [44], which was constructed by manually defining each tow's four spikes at peak amplitude points, was the tow path taken into consideration for this study. The chosen yarn path was also shown to be a good fit for characterise ultra thin woven fibre composites by previous studies [45]. Equation 3.4 presents the parametric equation of Cubic Bezier interpolation.

$$B(t) = P_0(1-t)^3 + 3P_1t(1-t)^2 + 3P_2t^2(1-t) + P_3t^3; \qquad 0 \leq t \leq 1 \tag{3.4}$$

where, t a parameter that represent point of the interpolation between two points, P_0, P_1, P_2, P_3 nodes defined on considered geometry (Figure 3.2). After applying idealised geometric parameters, equation 3.5 and 3.6 represent the specific tow architecture used in this study.

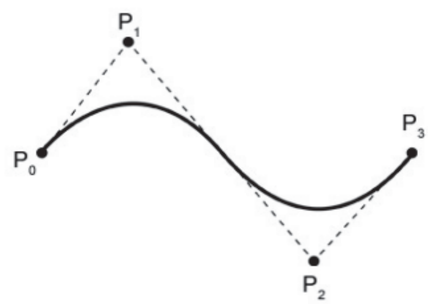

Fig. 3.2: Cubic Bezier interpolation

$$x(t) = -1.332t^3 + 1.998t^2 + 1.998t - 0.6661 \tag{3.5}$$

$$y(t) = 3.522t^3 - 5.282t^2 + 1.761 \tag{3.6}$$

Equation 3.7 used to calculate the total length of tow segment between pre-defined boundary nodes

$$Length = \int_0^1 \sqrt{(\frac{dx}{dt})^2 + (\frac{dy}{dt})^2}\, dt \tag{3.7}$$

3.1.2 Resin pocket

Resin pocket used in the resin embedded model is formulated only in the space between two plies in accordance with the specimens used in experimental studies which is fabricated under extremely controlled conditions. Mallikarachchi only used the exact volume which is only sufficient to fill the gap while fabricating two-ply plain woven composite [4]. Only a maximum thickness of 0.059 mm used for the embedded resin between two plies. Despite the fact that there can be a still thin film of resin on top of composite, that can be neglected in property characterisation, anticipating on inspecting strain ranges.

3.1.3 Fibre volume fraction

The Fibre Volume Fraction (V_f) of tows in the idealised model is a ratio that represents the entire volume of fibre inside the composite in actual scenario, voids excluded. Since the weighting approach was utilised to estimate the volume fraction of the considered experimental specimen, the fibre volume fraction employed in this study is derived by removing potential voids in the composite.

V_f = 0.62 was chosen to model tows in the dry fibre model, which was based on the assumption that the effect of whole fibre fraction utilised in the experiment is contributed exclusively of tows in idealised model.

The total volume of tows in the two-ply plain-woven RUC has been computed to be 1.1585 mm^3, using the length of a single tow in the RUC as 2.785 mm which is calculated with Equation 3.7.

Because of this, the following Equation 3.8 was used to compute the fibre volume fraction for the resin pocket contained model. The obtained value of 0.74 was applied to additional homogenised tow property computations that took into account the presence of an extra matrix while keeping the overall volume fraction at 0.62.

$$V_f = 0.62 \times \frac{Total\ volume\ of\ tows\ +\ Volume\ of\ resin\ pockets}{Total\ volume\ of\ tows} \tag{3.8}$$

3.2 Material Properties

Accurate material properties are paramount in fibre composite simulations, especially in aerospace-related applications, as these simulations underpin the structural integrity and performance of critical components. In aerospace, where weight, strength, and durability are vital, using precise material data—encompassing parameters like stiffness, strength, and fatigue resistance—is indispensable. The behaviour of composite structures under extreme conditions, such as high pressures, temperature variations, and dynamic loads, necessitates exact material properties for reliable predictions. Without this accuracy, the simulation's output may lead to sub-optimal designs, potentially compromising safety, efficiency, and the overall performance of aircraft, spacecraft, and related aerospace systems. Hence, ensuring the correct material properties is fundamental for developing robust and reliable composite structures within the stringent demands of the aerospace industry.

Composite laminate considered in this study was made of T300-1k carbon fibres and HexPly 913 epoxy. This section presents the methods used in calculating applied material properties in simulations.

3.2.1 Tow Properties - Linear Region

Tows are idealised as three-dimensional continuum with transversely isotropic material properties. To represent transversely isotropic continuum five independent engineering constants are required [7].

1. Longitudinal Young's modulus
2. Transverse stiffness
3. Shear stiffness
4. In-plane shear stiffness
5. Poisson's ratios

Above mentioned characteristics of the tows in materially linear region was calculated using Halpin-Tsai semi empirical relation, Rule of Mixtures [7] and using a method proposed by Song et. al., in 2008 [46].

Longitudinal extensional modulus (E) and Poisson's ratios (ν) and shear stiffness (G) values are obtained as below. E_1, ν_{12}, ν_{13} values are calculated directly using rule of mixtures and E_2, E_3, G_{12}, G_{13} estimated using Halpin-Tsai semi empirical equation.

$$E_1 = E_{1,f} + E_m(1 - V_f) \tag{3.9}$$

$$\nu_{12} = \nu_{13} = \nu_{12,f}V_f \ + \ \nu_{12,m}(1 - V_f) \tag{3.10}$$

$$E_2 = E_3 = E_m\frac{1 + X\eta V_f}{1 - \eta V_f} \tag{3.11}$$

where,

$$\eta = \frac{E_{2f} - E_m}{E_{2f} - XE_m} \tag{3.12}$$

Parameter X is a measure of reinforcement which is controlled by fibre geometry and loading conditions was considered as 2.0 [14]. Shear modulus was also calculated following the Helpin-Tsai semi emphirical equation.

As mentioned earlier, volume fraction of 0.62 was used for dry fibre model. Obtained linear region properties are presented in table below.

Tow property	$V_f = 0.62$	$V_f = 0.74$
Longitudinal Young's modulus, $E_1(N/mm^2)$	145,748	173,301
Transverse stiffness $E_2 = E_3(N/mm^2)$	10,427	13,099
Shear stiffness $G_{12} = G_{13}(N/mm^2)$	3,378	4,334
In-plane shear stiffness $G_{23}(N/mm^2)$	3,498	4,493
Poisson's ratio, $\nu_{12} = \nu_{13}$	0.28	0.26
Poisson's ratio, ν_{23}	0.49	0.45

3.2.2 Non-linear Material Behaviour of Fibre

The challenges associated with carbon fibre are undoubtedly distinct, but they are arguably no more serious than those associated with other contemporary materials. For instance. We have anisotropy in place of the issues with heat treatment, complicated alloys, and corrosion that metals face. limitations of the matrix and brittle fracture. In addition to being anisotropic, carbon fibre has a non-linear elastic response to strain.

This non-linear elastic response during tensile loading can be attributed to several microscopic structural changes such as local stress concentrations, phase transformations and strain localisation. At the microscopic level, the deformation mechanism in carbon fibres can be complex. Micro-structural irregularities or defects in carbon fibre itself can be lead to local stress concentration which cause non-linear deformations and hence contribute to the overall mechanical response. Also, non-uniform distribution of strain within microstructure can lead some regions to experience higher deformation than others. This phenomena can also contribute to the exhibited non-linear material properties.

It is crucial to comprehend and manage these micro-structural alterations in order to customise the mechanical properties of carbon fibre composite materials. In order to attain desired properties and minimise the impact of non-linearities, engineers and materials scientists optimize the micro-structure.

Regretfully, there is currently a lack of industry standardisation regarding the exact methodology to be employed; specifically concerning the gauge-length, area evaluation, and strain measurement technique. End-effects are problematic, especially when using high-modulus fibres.

Hughes [47] came up with a method based on standard tensile and compression tests to quantifying non-linear behaviour of single fibre filaments and presented results for carbon fibres in the strain range of near zero to near maximum (2%) using empirical formula,

$$E_f = E_0(1 + f.\varepsilon) \tag{3.13}$$

where, E_0 = modulus at zero strain; E_f = modulus at strain ε; f = factor depend on fibre type. For T300 fibre, a factor of 8 has been used in tension and 13 in compression[47].

3.2.3 Non-linear Material Behaviour of Resin

Unfortunately, non-linear stress strain behaviour for the Hex-Ply 913 resin which was used in the experiments was not provided by the manufacturer but the initial elastic modulus. Non-linear stress strain behaviour of the resin was calculated following the procedure outlined by Jayasekara et. al., [8]. The first step was to estimate the shear response of the resin itself using the composite shear stress vs. shear strain response that has already been determined through experiments. composite shear stress vs strain graph is shown in Figure 3.3.

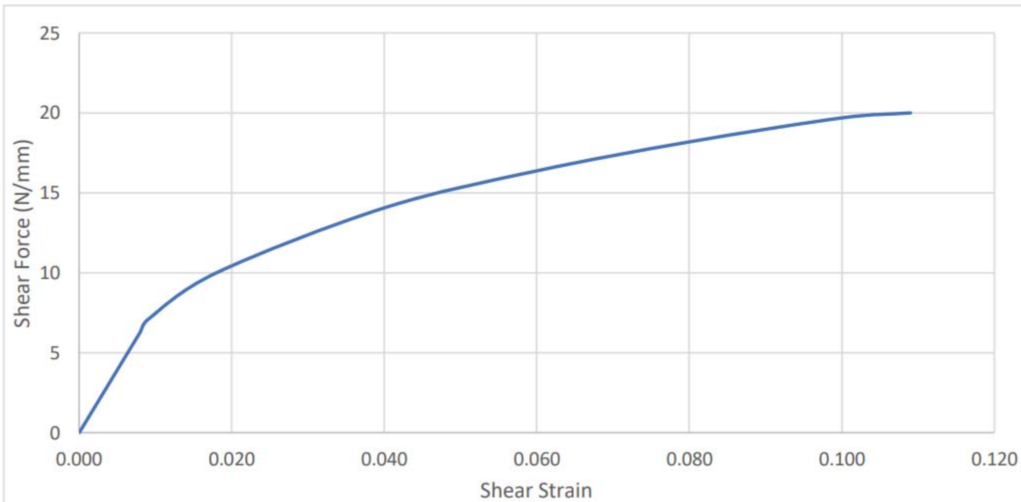

Fig. 3.3: Composite Shear stress vs Shear strain of Resin [8]

After that, the Halpin-Tsai semi-empirical relation was used to calculate the initial shear modulus of the resin. This resulted in a 2% difference between the shear modulus and the resin's technical data sheet. The secant shear modulus was then used to expand this process to the non-linear region. The secant shear modulus of resin was then used to determine the full non-linear shear response of the material. Obtained shear stress vs strain response for resin itself is showed in Figure 3.4.

Then, using J_2 deformation theory of plasticity, estimated the equivalent stress and plastic strain for the resin using Equations 3.14 and 3.15.

$$\sigma = \sqrt{3J_2} = \sqrt{3S\ \ S\ } = \sqrt{3}\tau_{12} \tag{3.14}$$

$$\epsilon\ \ = \sqrt{\frac{2}{3}\epsilon\ \ \epsilon\ } = \frac{\gamma_{12}}{\sqrt{3}} \tag{3.15}$$

For the calculation, it was assumed that the non-linear response of the resin can be represent alone by the shear behaviour of resin. Obtained equivalent stress strain relationship for the resin itself is shown in Figure 3.5

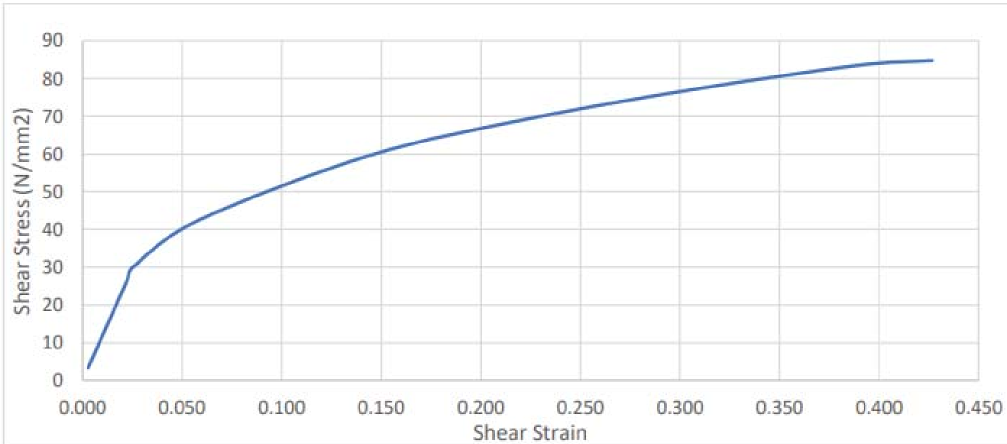

Fig. 3.4: Resin Shear stress vs Shear strain [8]

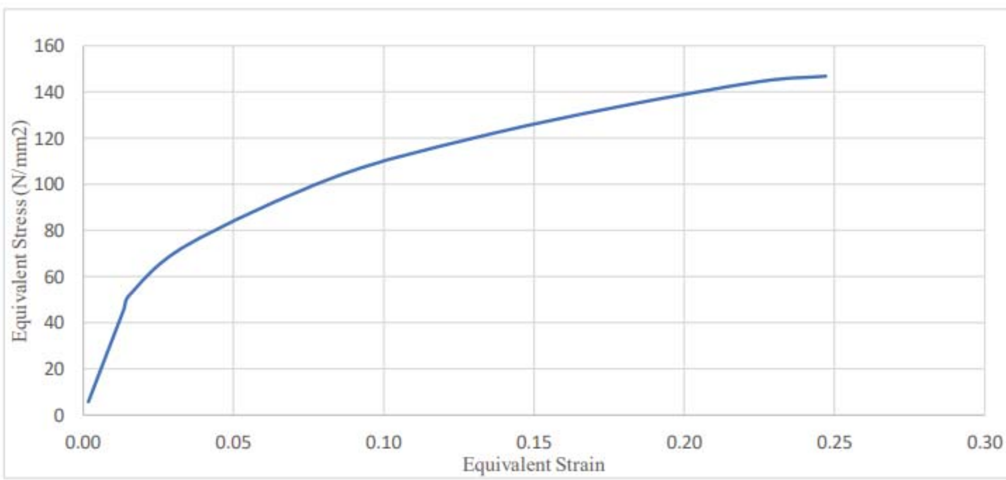

Fig. 3.5: Resin equivalent stress vs strain relationship [8]

3.2.4 Tow properties - non-linear region

One important factor that severely affects the mechanical performance of composite materials is the non-linear behaviour of carbon fibre tows. Conforming to literature, carbon fibre tows, shows an unique stress-strain response that differs from the linear Hookian behaviour typical of conventional materials.

This type of non-linearity is not usually considered when designing thick composite parts due to their functions lies at relatively lower strains; however, thin composites that are bending may experience significant strains, as in the case of deployable structures [48]. Since we are focusing on the behaviour of thin woven composites in aerospace applications in this study, it is significant to consider the effect of material non-linearity for overall behaviour.

The non-linear elastic behaviour of both carbon fibres and resin was reported as early as 1960's and then more recently. Numerous elements contribute to this non-linearity, such as the complex microstructure, interactions within the composite matrix, and the intrinsic anisotropic nature of carbon fibres. The stress-strain relationship may diverge from a linear trajectory with increasing strain, leading to phenomena such as interfacial debonding, fibre sliding, and matrix cracking,.

An extra contributing factor could be the original waviness in the fibres that resulted from the manufacturing process' curing step. The undulation of fibres inside a tow is referred to as fibre waviness. When under tension, the misaligned fibres ought to straighten and completely contribute to the uni-directional stiffness of the tow. Conversely, as compression occurs, these fibres ought to flex more and more, reducing the uni-directional stiffness of the tow under load [48].

The non-linearity resulting from the pure material non-linear behaviour of the tows' constituents (i.e., T300 carbon fibre and Hex-Ply 913 Resin) is the main focus of this study; however, the non-linearity resulting from matrix cracking or undulation is not taken into account.

This non-linear behaviour is not taken into account for design of thick composite parts or for composites in general applications. But, when it comes to deployable structures in aerospace applications, it plays a significant role since they undergo large strains in bending. In this study, we investigate the effect of non-linearity in the fibre stiffness on the mechanics of laminate.

Both fibre component and resin component are assumed to be non-linear for the considered strain interval. Variation of fibre extensional modulus with respect to applied strain is considered as Equations 3.16 and 3.17 referring to Ajay et. al,[5].

$$E_{f,T} = E_0(1 + \gamma_T.e)\ for\ \epsilon >= 0 \tag{3.16}$$

$$E_{f,C} = E_0(1 + \gamma_C.e)\ for\ \epsilon <= 0 \tag{3.17}$$

Longitudinal extensional modulus and the poisons ratio was calculated for the tows following rule of mixtures. Since the equation considered in rule of mix established based on average stresses act on cross sectional areas, it is applicable for the non-linear region as well [7]. Also, longitudinal Young's modulus can be regarded as a fibre dominated property since we are using a higher fibre volume fraction and hence non-linear behaviour in fibre contribute to E_1 extremely. Figure 3.6 shows the uni-directional stiffness values used for the considered strain range. Despite the fact that

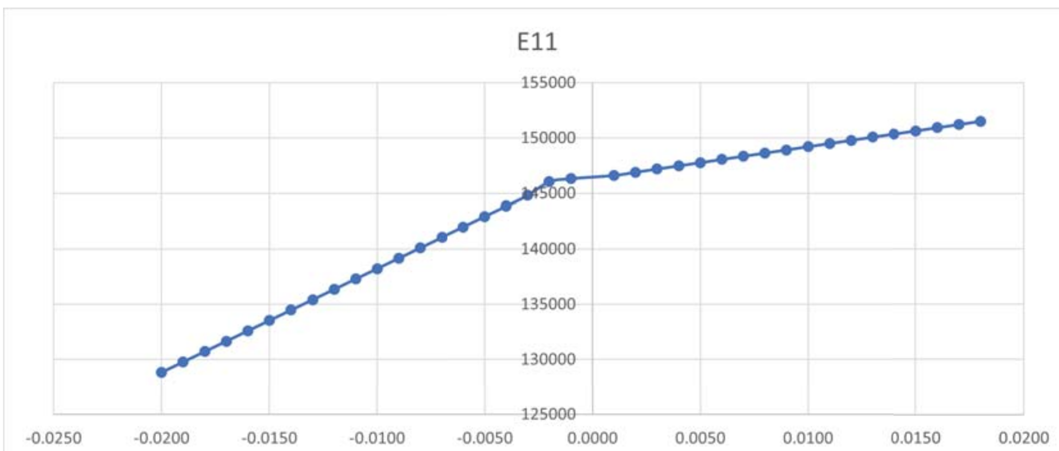

Fig. 3.6: Non-linear variation of tow axial stiffness

the concept of Poisson's ratio can be extended to the non-linear region the deviation can be negligible for carbon fibres [49]. Major Poisson's ratio ν_{12} is obtained by an approach similar to analysis for E_1. Since the major Poisson's ratio is for the stress state $\sigma_1 = \sigma$ while other stresses are zero. For non-linear region we are assuming a constant major Poisson's ratio, we can obtain ν_{12} with the same procedure as rule of mixtures for the considered strain range.

$$\nu_{12} = \nu_{13} = \nu_{12,f}V_f\ +\ \nu_{12,m}(1 - V_f) \tag{3.18}$$

For the rest of the properties such as transverse stiffness, and both in-plane and out of plane shear stiffness was assumed constant through the entire regions since the main focus of the study was to evaluate the effect of uni-directional material non-linearity of tows for mechanical behaviour of ultra-thin plain woven composites.

3.3 Interaction Properties

Improving interconnection behaviour between contact regions was one of the study's primary goals. The hypothesis was that the extreme curvatures that these ultra-thin woven composites are subjected to may cause slipping behaviour between plies and between yarns, which would reduce the bending stiffness at those higher curvatures.

In order to mimic contact behaviour there are two approaches offered by Abaqus standard software package. Surface-based cohesive contact behaviour or cohesive elements are to be used. Cohesive elements serve as the link between two dissimilar components. Usually, the cohesive parts completely break down under tension and/or shear as a result of the deformation. Substantial adhesion between cohesive components may develop from their initial interaction.

In Abaqus/Standard, the cohesive surface behaviour can also be designated as a surface interaction property for contact surfaces. The three characteristics listed below specify the formulas and governs the surface-based cohesive behaviour:

1. Linear elastic traction - separation
2. Damage initiation criteria
3. Damage evolution laws

Figure 3.7 shows the cohesive law, which is the constitutive relationship between traction and separation of the cohesive surface. Three components—two transverse shear and one through thickness component—combined to form the cohesive law and describe traction and separation between two surfaces.

To simulate traction separation behaviour, coefficient values were obtained from a previous study by Wijesuriya et. al, [38]. In that study, a matrix block modelled in the ABAQUS finite element package was used to idealize fracture behaviour in the normal direction. The block had a pre-introduced 0.5 mm crack that ran the full thickness of it, measuring 1 mm $\times$ 2 mm $\times$ 0.01 mm (Figure 3.8).

The Extended Finite Element Modelling (XFEM) approach, which is the foundation of Linear Elastic Fracture Mechanics (LEFM), was used for the simulation.

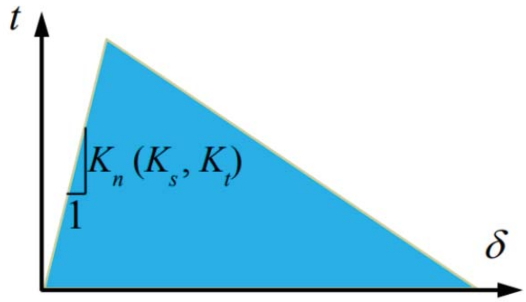

Fig. 3.7: Traction separation behaviour for contact surfaces[9]

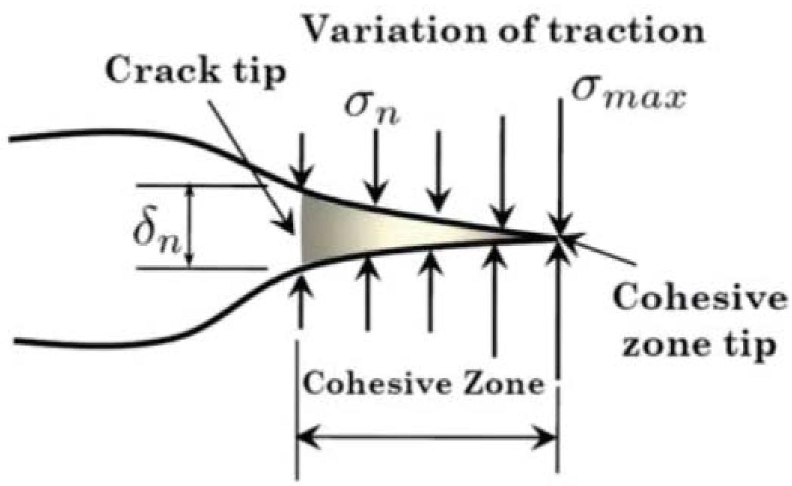

Fig. 3.8: Extraction of opening displacement and normal stress at crack tip[38]

Manufacturer data was used to determine the specimen's tensile strength and material properties. An arbitrary load was then applied. XFEM facilitated the simulation of crack initiation and propagation without the need for re-meshing, in contrast to traditional FEM. Normal traction stiffness (K_{nn}) was found to have an estimated value of 253,722 MPa/mm. Furthermore, by utilizing the connection between (K_{nn}) and material characteristics, the shear moduli ((K_{ss}) and (K_{tt})) were estimated. Because of the resin material's homogeneity and isotropy, both (K_{ss}) and (K_{tt}) considered eqaul and have a value of 90,561 MPa/mm.

CHAPTER 4

NUMERICAL MODELLING

This chapter elaborates on the theories and procedures used in the development of the RUC using the Abaqus finite element software package and the analysis method.

This study employs a dry fibre architecture to model fibre composites, as it more closely represents the realistic geometry of the material. The aim is to assess whether capturing this realistic geometry leads to more accurate simulation results, particularly in contact regions. To further examine the influence of material non-linearity on the observed reduction in bending stiffness, both linear and non-linear material analyses were conducted within the geometrically non-linear regime.

Everything is covered, including geometric modelling and selecting the right analysis methods. Providing a viewpoint on creating meso-level unit cell models for ultra-thin woven composites and analyse it with both linear and non-linear material properties in the geometric non-linear region is the primary objective.

4.1 Geometric modelling

Prior to being meshed in a finite element package, geometric models need to be ready and unit cell architecture should be precisely described. Selecting the fundamental representative volume element (unit cell) is important because it should neither be overly complex to raise the computational cost of the model nor too simple to overlook specifics of the analysis or findings in the conclusions.

The composite that we have considered in this study was plain woven architecture and it is comprised of the most basic pattern. We have defined the appropriate 2×2 RUC considering the pattern of repetition of woven composite. Dimensions of the repetitive pattern were taken as 2.664 mm × 2.664 mm which is the wavelength of the tows as observed in micrographs [14]. Despite the fact that these can be phase differences in two plies for the tow arrangement, only fibre in-phase configuration is used in this study based on the findings by Gowrikanthan et al., [43] stating that the effect of phase difference towards predicting bending stiffness is not significant.

4.1.1 Dry fibre model

A realistic depiction of the tow architecture in the RUC is necessary for the prediction of the mechanical properties of textile composites. The tow geometry of the RUC was developed using the finite element pre-processor TexGen, which is readily available. The definitions of tow length, cross section, and tow path are presented in Chapter 03.

Tows were modelled using eight-node linear reduced integration brick elements (C3D8R). Also, discretisation was carried out through TexGen, the above mentioned finite element pre-processor. Having four mesh layers in the tow cross-section and sixty section points around the circumference enhanced the density of the mesh. Note that the mesh sensitivity analysis was carried out earlier using different mesh sizes first and the most optimum mesh with convergence of results and acceptable computational cost was used to determine the number of section points.

Layers of four through thickness element were utilised to increase precision and prevent hour glassing effect of the elements. There will only be one or two integration points through the thickness if there are fewer mesh layers since reduced integration elements are used in this simulation. This will prevent it from accurately record the deformations, particularly while bending, which could result in a zero energy mode. The mesh layers were increased using the built-in Python console; the Python codes employed are listed in Appendix 01.

If there were overlapping elements between the meshes of two tows at the contact regions that would lead to mesh distortion and skewed elements that could cause outliers in the results. For accurate findings and realistic contact behaviour, these overlapping zones must be treated properly. Overlapping items were identified as mistakes during pre-processing using Tex-GEN pre-processor and fixed before the analysis may continue utilising the built-in tool to "Adjust intersections"[44], which makes minuscule, local adjustments to the volume mesh until the intersections are within the selected intersection tolerance of overlapping (Figure 4.1), allowed for the reinforcement of the cross-over regions, which had been a challenge in creating the complex geometry. The employed tolerance value was 0.005 mm, which is less than the mesh's single element dimensions.

After that, the model was exported as an '*.inp' input file. Then Abaqus FE software package was used to execute the input file and import it as an orphan mesh. In

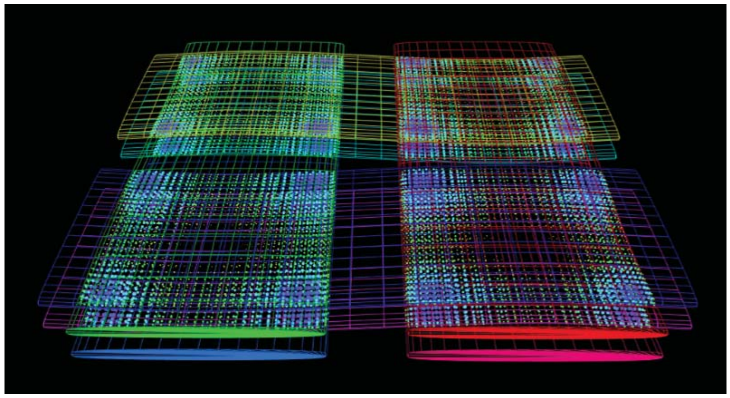

Fig. 4.1: Identified interpenetration at contact regions using TexGEN

Abaqus, each tow was assigned a set of tow parameters, which were determined using a 0.62 fibre volume fraction as discussed in Chapter 03.

4.1.2 Interaction between contact surfaces

Enhance the mimicking of tow interconnection behaviour to accurate prediction of bending stiffness reduction was one of the investigation's primary goals. The extreme curvatures that these ultra-thin woven composites are subjected to could lead to slippage behaviour between plies and between tows, which would cause the observed bending stiffness. To check our hypothesis that this tow slippage concept could be an important if not the dominant dynamic associated with the observed bending stiffness reduction, accurate modelling of interaction behaviour was an essential requirement.

To model inter-slippage between two contact surfaces, Abaqus provides two different approaches specified as surface based contact behaviour and element based contact behaviour. Element based contact behaviour is more effective in modelling comparatively small and less complex contact surfaces which more localised contact phenomena is dominant since the computational cost is expensive [9]. Surface based contact behaviour can be applied in complex contact behaviours with sufficiently fine enough mesh to capture the accurate behaviour which is employed in our proposed model.

In this case, thicknesses of the interaction zones between the tows are remarkably thin, and the geometric architecture of the composite is extraordinarily complex making that challenging to define a mesh between contact regions. Since improper mesh will be resulted in distortion of elements in a element based cohesive behaviour and the quality of surface mesh alignment turned out in this study lead us to utilise a surface based contact behaviour with cohesive constrains characterised by linear elastic traction-separation behaviour calculated to simulate the actual effect of resin as described in Chapter 03. Note that the damage initiation and propagation was not considered in the study.

In the proposed RUC there are 12 contact regions, 8 contact regions between tows in the same-ply and 4 contact regions at the cross-over points of two plies. For each contact region, both master and slave surface was selected manually using the orphan mesh element surfaces. Figure 4.2 shows a manually selected contact surface in the dry fibre model. Ultimately, to reduce the significant penetration of slave nodes, "Surface to surface" discretisation rather than the usual "Node-to-surface" discretisation was applied at the contact regions. Bi-linear traction separation law served as the foundation for defining the interface behaviour of surface-based cohesive contact.

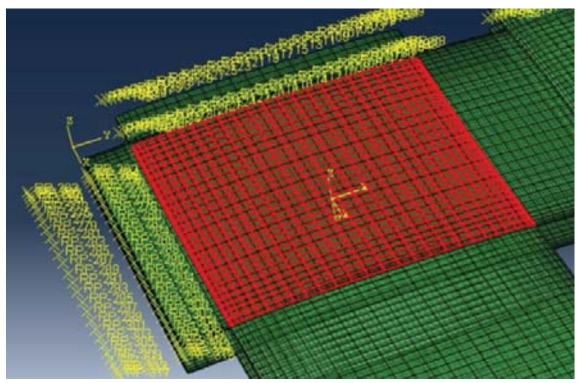

Fig. 4.2: Defined contact surface using mesh element surfaces

4.2 Multi-scale Modelling Techniques

Multi scale approaches generally seek to predict the macroscopic properties of engineered materials by modelling the underlying micro-structures' fundamental physics and mechanics in a methodical and consistent manner. In most of the multi scale modelling techniques, different scales are linked in the same part of the domain. Link between different scales are established through volume averaging of field variables. Then the modelling techniques are used in a way that different scales are solved parallel to achieve the global equilibrium. In this study, we have only focused on two-scales where micro (fabric scale) and meso(RUC scale) scales of woven composites are involved. Conventional loop strategy for two-scale problem is illustrated in Figure

4.3 and, F_M, P_M and C_M refers to the macro-scale deformation gradient, First Piola-Kirchhoff stress and material constitutive tensor, respectively.

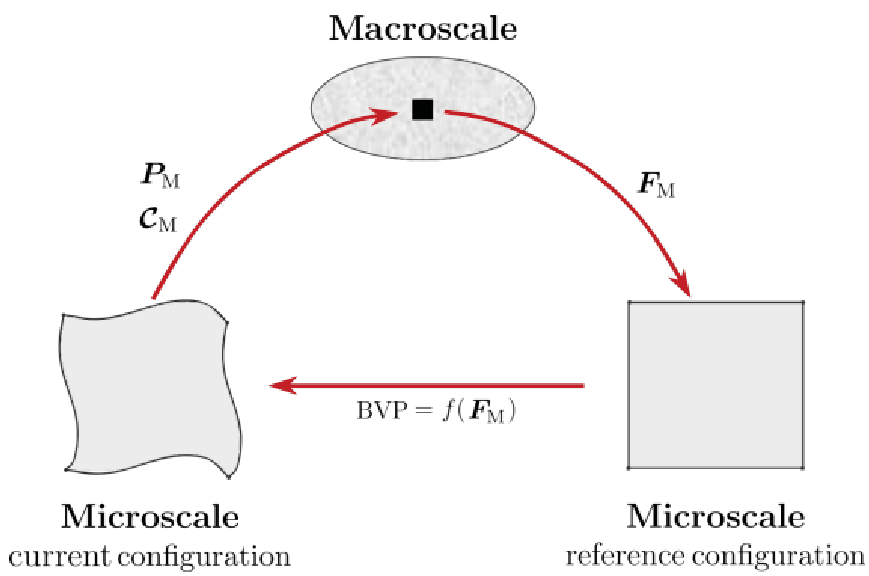

Fig. 4.3: Computational homogenization for two-scale problem

In addition to having the potential to become anisotropic and non-linear, the composite under investigation also has a tendency to be locally heterogeneous. Thus, we systematically extract the constitutive response numerically from controlled simulations of a mesostructural RUC in order to solve the macro-scale equilibrium equation as a computational homogenisation technique. Section 4.1 describe the modelling of representative unit cell and this section will describes the techniques that is used in kinematical coupling of meso and macro scales.

Developing expressions to couple the mesoscale deformation gradient to the macro-scale deformation gradient is the first phase involved. In this case, variations in any arbitrary macro-scale position vector is expressed using the Taylor expansion. Any position vector in the reference configuration is denoted as **X** and corresponding position vector in the deformed configuration is denoted as **x**. If the meso-structural contribution on macro-scale is augmented by an additive component ω, for any computational homogenisation strategy,

$$\Delta x = \omega + F_M.\Delta X + \frac{1}{2}\Delta X.(\Delta_M.F_M).\Delta X + ... \tag{4.1}$$

for this study, we only consider the first-order computational homogenisation that simplify the Equation 4.1 to following equation.

$$\Delta x = \omega + F_M.\Delta X \tag{4.2}$$

4.2.1 Boundary Conditions

Boundary conditions in a computational homogenisation problems are significant since they provide the representativeness, size effect and the convergence of results. We distinguish between three primary boundary enforcement strategies that are frequently employed in the fields of computational homogenisation. Those are,

1. Displacement boundary conditions
2. Traction boundary conditions
3. Periodic boundary conditions

In order to apply boundary conditions, kinematic variables were first defined as in theory of laminated plates. Continuum composite represented by a repetitive unit cell was then idealised as a thin shell using Kirchhoff-Love hypothesis to obtain the constitutive relationship. In plane deformations were described using first order Taylor series (Equation 4.3, Equation 4.4) and out-of-plane deformations were described using second order Taylor series(Equation 4.5).

$$u = u_0 + \epsilon_x x + \frac{1}{2}\epsilon_{xy} y \tag{4.3}$$

$$v = v_0 + \epsilon_y y + \frac{1}{2}\epsilon_{xy} x \tag{4.4}$$

$$w = w_0 + \left(\frac{\partial w}{\partial x}\right)_0 x + \left(\frac{\partial w}{\partial y}\right)_0 y + \frac{1}{2}\left(\frac{\partial^2 w}{\partial^2 x}\right)_0 x^2 + \frac{1}{2}\left(\frac{\partial^2 w}{\partial^2 y}\right)_0 y^2 + \left(\frac{\partial^2 w}{\partial x \partial y}\right)_0 xy \tag{4.5}$$

from those, Kinematic variables for RUC were defined as,

$$\epsilon_x = \frac{\partial u}{\partial x} \tag{4.6}$$

$$\epsilon_y = \frac{\partial v}{\partial y} \tag{4.7}$$

$$\epsilon_{xy} = \frac{\partial u}{\partial y} + \frac{\partial v}{\partial x} \tag{4.8}$$

$$\kappa_x = -\frac{\partial^2 w}{\partial x^2} \tag{4.9}$$

$$\kappa_y = -\frac{\partial^2 w}{\partial y^2} \tag{4.10}$$

$$\kappa_{xy} = -2\frac{\partial^2 w}{\partial x \partial y} \tag{4.11}$$

where the x and y are the two in-plane principal directions and u, v and w are displacements in x, y and z directions respectively. It should be noted that the engineering shear strain and twice the surface twist are used to define the shear strain and twisting curvature respectively as in theory of laminated plates

For this study, periodic boundary conditions were applied to the representative unit cell to simulate the continuum nature of the composite. Considering the local periodicity of RUC, general form of periodic boundary conditions can be written as,

$$x_M^+ - x_M^- = F_M.(X_M^+ - X_M^-) \tag{4.12}$$

to fulfill the requirement of Equation 4.12, micro-fluctuations (w_m) and the normal vectors at the boundary to be anti-periodic. Hence,

$$w_m^+ - w_m^- \tag{4.13}$$

$$n_m^+ - n_m^- \tag{4.14}$$

Adhering to the above mentioned equations, following equations suggested by Mallikarachchi [14] were enforced in the mesoscale model using equation constraints to the pre-defined reference nodes and dummy nodes.

$$\Delta u^x = \epsilon_x \Delta L \tag{4.15}$$

$$\Delta v^x = \frac{1}{2}\gamma_{xy}\Delta L \tag{4.16}$$

$$\Delta u^y = \frac{1}{2}\gamma_{xy}\Delta L \tag{4.17}$$

$$\Delta v^y = \epsilon_x \Delta L \tag{4.18}$$

$$\Delta w^x = -\frac{1}{2}\kappa_{xy} y \Delta L \tag{4.19}$$

$$\Delta w^y = -\frac{1}{2}\kappa_{xy} x \Delta L \tag{4.20}$$

$$\Delta \theta_x^x = -\frac{1}{2}\kappa_{xy} \Delta L \tag{4.21}$$

$$\Delta \theta_y^x = \kappa_x \Delta L \tag{4.22}$$

$$\Delta \theta_x^y = -\kappa_y \Delta L \tag{4.23}$$

$$\Delta \theta_y^y = \frac{1}{2}\kappa_{xy} \Delta L \tag{4.24}$$

$$\Delta \theta_x^z = 0 \tag{4.25}$$

$$\Delta \theta_y^z = 0 \tag{4.26}$$

where, ΔL is the width of RUC and θ is the rotation. Here, superscript denotes the deformation direction and subscript denotes the direction of a paired boundary node. It should be noted that the engineering shear strain and twice the surface twist are used to define the shear strain and twisting curvature respectively as in theory of laminated plates.

For straightforward application of earlier mentioned equation boundary conditions, reference nodes were defined for each two tows in different plies which are in the same phase. For each aligned couple of above mentioned reference nodes at opposite sides, we have defined dummy nodes to link reference nodes in application of equation constraints. Note that all the reference odes and dummy nodes were defined in the neutral plane of the RUC to avoid imposing any additional moment during the simulation. Mesh element nodes at the boundary of both tows were selected by implementing a python code in Abaqus and connected to the corresponding reference node using MPC beam connectors. MPC beam connectors couple both translational and rotational degrees of freedom between connected points in a rigid of flexible manner. In this case, to transform applied strains directly to tows, we have rigidly coupled all DoFs between reference nodes and boundary nodes.

By imposing PBC, the homogenised Kirchhoff-Love plate theory idealises the RUC's behaviour. These PBCs are enforced by the Abaqus/Standard FE program through the use of *EQUATION constraints. Required two degrees of freedom for the

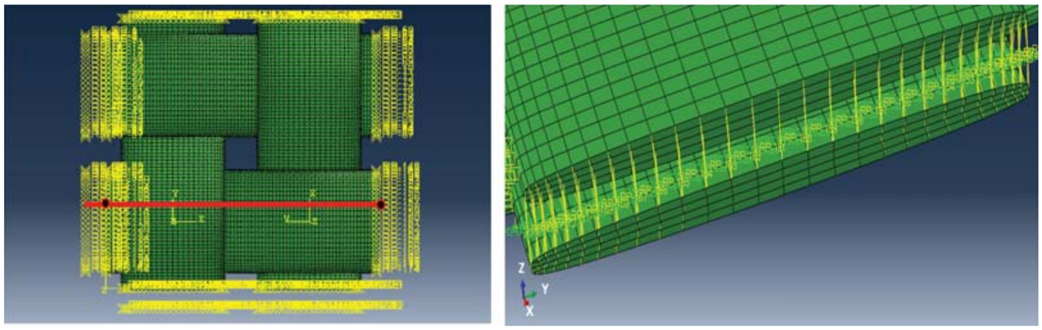

Fig. 4.4: Defined reference nodes and dummy nodes to apply PBC

*EQUATION constraints were enforced using the prescribed reference nodes and the nodal displacement that links two DOFs were enforced using corresponding dummy nodes.

Consequently, it allows to apply strains directly to the dummy nodes throughout the simulation. Defining reference nodes and dummy nodes per each couple of boundary nodes instead of connecting all boundary nodes to a single reference node eliminated both rigid plate behaviour at boundaries and the imposed local changes in tow cross section areas.

4.2.2 Formation of ABD matrix

As discussed earlier in Chapter 2, stress-strain relationship for an anisotropic material in general can be represented by a 6×6 stiffness matrix or a 6×6 compliance matrix. In context of composite material, ABD matrix can be define the key constitutive relationship between kinematic variables (mid plane strains and curvatures) and static variables (mid-plane forces and moments per unit width) using CLT. Due to the symmetry of stiffness and compliance tensors, this relationship require total 21 independent parameters to describe the material behaviour.

In a concise form ABD matrix is defined as,

$$\begin{Bmatrix} N \\ M \end{Bmatrix} = \begin{pmatrix} A & B \\ B & D \end{pmatrix} \begin{Bmatrix} \epsilon \\ \kappa \end{Bmatrix} \tag{4.27}$$

where N is the force per unit length, M is the moment per unit length, ϵ is the mid-plane strain, κ is the mid-plane curvature, [A] sub-matrix denotes the extensional stiffness matrix, [B] sub-matrix denotes the extension-bending coupling matrix, and [D] sub-matrix denotes the bending stiffness matrix.

Unit strain analysis has been performed first in the geometric linear region and calculated the ABD matrix using the principle of virtual work and then extended the analysis into geometrically non-linear region to calculate bending stiffness at higher curvatures. Note that the FE model was validated using the results of linear analysis and geometrically non-linear analysis was performed on the validated model.

All the strains and curvatures was applied to the model using prescribed dummy nodes. Displacements and rotations of each dummy node and corresponding forces and moments of reference nodes were extracted using output requests and a MATLAB code was utilised to calculate read and post process those results to obtain ABD matrix.

4.2.3 Principle of virtual work

For the linear analysis, 6-separate analysis for each unit deformation was performed while keeping all other deformations at zero (i.e, when $\epsilon_x = 1$, ϵ_y = γ_{xy} = κ_x = κ_y = κ_{xy} = 0). For the geometric non-linear analysis, a 0.2 mm^{-1} curvature value was imposed on the RUC as a ramp. All the above mentioned outputs for the geometrically non-linear analysis were extracted in equal time intervals to plot bending moment per unit width value vs applied curvature throughout the analysis. Applied curvature after each time period was calculated linearly interpolating between each time interval since the application of curvature was done in a linear manner.

Each of these analysis were referred to as case A to case F. Case A represent the condition where ϵ_x is given a predefined deformation and all other deformations set to zero. Simillarly, cases B,C,D,E,F refers to the cases where ϵ_y,γ_{xy},κ_x,κ_y,κ_{xy} subjected to predefined deformation respectively. As described earlier, from each analysis, extracted one set of displacements and rotations of the boundary nodes and corresponding forces and moments of dummy nodes. Then the principle of virtual work has been utilized to calculate each entity of the ABD matrix. For $ABD_{1,1}$, virtual work calculation for case A is as follow,

$$N_{xx}\epsilon_{xx}\Delta l_x \Delta l_y = \sum \left(F_x u + F_y v + F_z w + M_x\theta_x + M_y\theta_y + M_z\theta_z\right) \tag{4.28}$$

Summation is defined for all boundary nodes and ϵ_{xx} has been substituted by $\epsilon_{xx} =$

1 for the linear analysis and applied corresponding strain for the non-linear analysis. In this case, it was $\epsilon_{xx} = 0.2$. Principle work equations for all six analysis has been listed and converted into tensor form to calculate the ABD matrix directly. In that case, three displacements and three rotations for each 1392 boundary nodes has been combined in to the displacement matrix U(1392×6) and corresponding forces and couples of each boundary nodes has been combined in to the force matrix F(1392×6) for each particular case as follows.

$$U = \begin{bmatrix} u_{P_1A} & u_{P_1B} & u_{P_1C} & u_{P_1D} & u_{P_1E} & u_{P_1F} \\ v_{P_1A} & v_{P_1B} & v_{P_1C} & v_{P_1D} & v_{P_1E} & v_{P_1F} \\ w_{P_1A} & w_{P_1B} & w_{P_1C} & w_{P_1D} & w_{P_1E} & w_{P_1F} \\ \theta_{P_{1x}A} & \theta_{P_{1x}B} & \theta_{P_{1x}C} & \theta_{P_{1x}D} & \theta_{P_{1x}E} & \theta_{P_{1x}F} \\ \theta_{P_{1y}A} & \theta_{P_{1y}B} & \theta_{P_{1y}C} & \theta_{P_{1y}D} & \theta_{P_{1y}E} & \theta_{P_{1y}F} \\ \theta_{P_{1z}A} & \theta_{P_{1z}B} & \theta_{P_{1z}C} & \theta_{P_{1z}D} & \theta_{P_{1z}E} & \theta_{P_{1z}F} \\ \ldots & \ldots & \ldots & \ldots & \ldots & \ldots \\ \theta_{S_{348z}A} & \theta_{S_{348z}B} & \theta_{S_{348z}C} & \theta_{S_{348z}D} & \theta_{S_{348z}E} & \theta_{S_{348z}F} \end{bmatrix} \tag{4.29}$$

$$F = \begin{bmatrix} F_{P_{1x}A} & F_{P_{1x}B} & F_{P_{1x}C} & F_{P_{1x}D} & F_{P_{1x}E} & F_{P_{1x}F} \\ F_{P_{1y}A} & F_{P_{1y}B} & F_{P_{1y}C} & F_{P_{1y}D} & F_{P_{1y}E} & F_{P_{1y}F} \\ F_{P_{1z}A} & F_{P_{1z}B} & F_{P_{1z}C} & F_{P_{1z}D} & F_{P_{1z}E} & F_{P_{1z}F} \\ C_{P_{1x}A} & C_{P_{1x}B} & C_{P_{1x}C} & C_{P_{1x}D} & C_{P_{1x}E} & C_{P_{1x}F} \\ C_{P_{1y}A} & C_{P_{1y}B} & C_{P_{1y}C} & C_{P_{1y}D} & C_{P_{1y}E} & C_{P_{1y}F} \\ C_{P_{1z}A} & C_{P_{1z}B} & C_{P_{1z}C} & C_{P_{1z}D} & C_{P_{1z}E} & C_{P_{1z}F} \\ \ldots & \ldots & \ldots & \ldots & \ldots & \ldots \\ C_{S_{348z}A} & C_{S_{348z}B} & C_{S_{348z}C} & C_{S_{348z}D} & C_{S_{348z}E} & C_{S_{348z}F} \end{bmatrix} \tag{4.30}$$

here, P,Q,R,S refers to the first letter of label name used to identify which side of the RUC the node is belongs to. According to that, R and S refers to the opposite sides of P and Q respectively. Matlab algorithm has been developed to construct above matrices from extracted node outputs and Equation 4.31 used to calculate ABD matrix from U and F.

$$ABD = \frac{U \quad F}{\Delta l \ \ .\Delta l} \tag{4.31}$$

4.3 Incorporate Material Non-linearity in RUC

As discussed in the preceding chapter, behaviour of ultra thin woven composite materials are significantly differ from the assumptions made in traditional mechanics of composites in two aspects. First, these thin woven composites exhibit extremely higher strains which can be only observed in thin composites under bending. These strains are approximately two-three times larger than the strains that can be observed in thick composites of the same material [50]. Secondly, carbon fibres demonstrate highly non-linear, yet elastic behaviour at these large strains. Several non-linear elastic constitutive models have been proposed for carbon fibre axial behaviour. These models accurately describe the behaviour over large strains and are more effective when tension and compression are considered separately.

As described in the previous Chapter, bimodal constitutive model was assumed to represent tows which allows stress to be a quadratic function of strain in both tension and compression with the same slope at zero strain. Equation 4.32 is utilised to represent the tow behaviour which is suggested by Thomas [50].

$$\begin{aligned} &E(\epsilon) = V\ \ (E\ \ [\epsilon < \epsilon\ \ \ ] + E_0(1+\gamma\ \epsilon)[\epsilon\ \ \ < \epsilon < 0] + E_0(1+\gamma\ \ \epsilon)[0 < \epsilon < 0]) \\ &+(1 - V\ \ )E\ \ \ \ \ \ (\epsilon) \end{aligned} \tag{4.32}$$

where, E_0 is the modulus at zero strain, $[\epsilon]$ notation is used to indicate a step function that is one if the enclosed condition is true and 0 if the condition is false. Here, E modify the model to allow modulus to drop to positive near zero at a critical value of compressive strain. However, In this study, observed maximum compressive strain was lower than the critical compressive stress and hence not leading to near zero axial stiffness (Figure 3.6).

To model this kind of complex material behaviour, it is essential to combine theoretical constitutive models and experimental data in numerical simulations. Commercially available ABAQUS FEM package provide different options to model hyperelastic material of this nature such as, built in material models (Mooney Rivlin, Ogden), experimental data fitting models, material calibration methods and user material subroutines.

In this study, we have utilised user defined subroutine to model the material behaviour based on Equation 4.32 since built in material models cannot represent this behaviour neither experimental data was available to calibrate the material.

Figure 4.5 shows the basic flow of data from start of an ABAQUS analysis to end of a step, In this figure, green boxes signifies a decision point or specific state in the analysis and blue colour boxes signifies an action taken during the analysis.

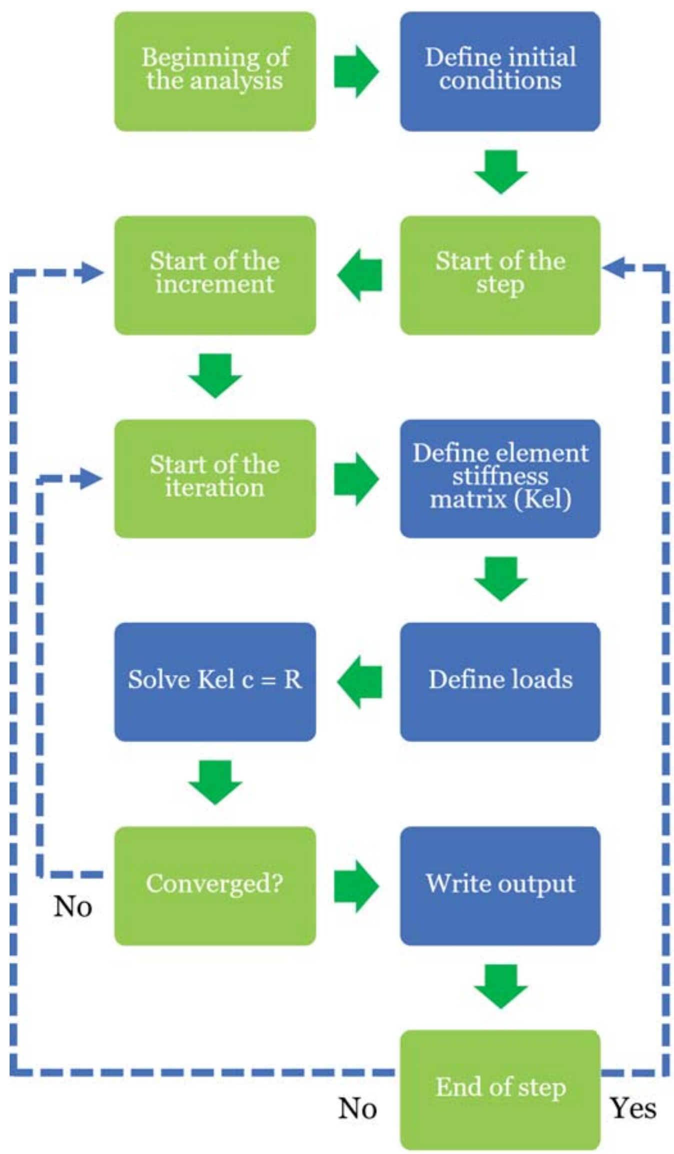

Fig. 4.5: Global flow in ABAQUS

User subroutines which are used in modify material behaviour are normally called at the start of an iteration. During the first call, initial stiffness matrix is formed using the model configuration at the start of the increment and during the second call, new stiffness matrix based on the updated configuration is created. In subsequent iterations, subroutines are called only once. It should be noted that in these iterations, model configurations are always calculated using the stiffness matrix from the end of the previous iteration.

4.3.1 USDFLD Subroutine

USDFLD subroutine has access to solution data after each increment which allow to define material properties as a function of solution data (i.e. $f_i(\sigma, \epsilon, \epsilon', etc)$. This subroutine has been used in this study to extract field variable values at current material points that were interpolated from the nodes at the end of current increment. Updated field variable values are used in calculating values of material properties that are defined as a function of field variables (Figure 4.6). The input form of the function can be either tabular or additional user subroutines.

In this study, axial stiffness (E_{11}) for tows has been inputted as a function of axial strain in tabular form for the strain range of [-0.02, 0.02] with a 0.001 gap between two data points. Inputted strain range was determined by performing a simulation for the same curvature without introducing material non-linearity and obtaining the maximum compressive and tensile stress induced throughout the simulation. Note that ABAQUS will use linear interpolation between data points in the tabular input and will use the last available material data if the field variable value is outside of the specified range and will not extrapolate.

Since the USDFLD subroutine has access to the material point quantities only at the start of an increment, the solution dependence introduced in this way inside the increment is explicit and hence the material properties for a given increment will not influenced by the results obtaining during the increment. Therefore, in order to achieve the required accuracy, time increment should be controlled manually. Automatic time incrementation algorithm defined in ABAQUS will reduce the time increment size when convergence is unlikely or the results are not accurate enough. Using PNEWDT function, we set large enough time increment value before each call to USDFLD thus

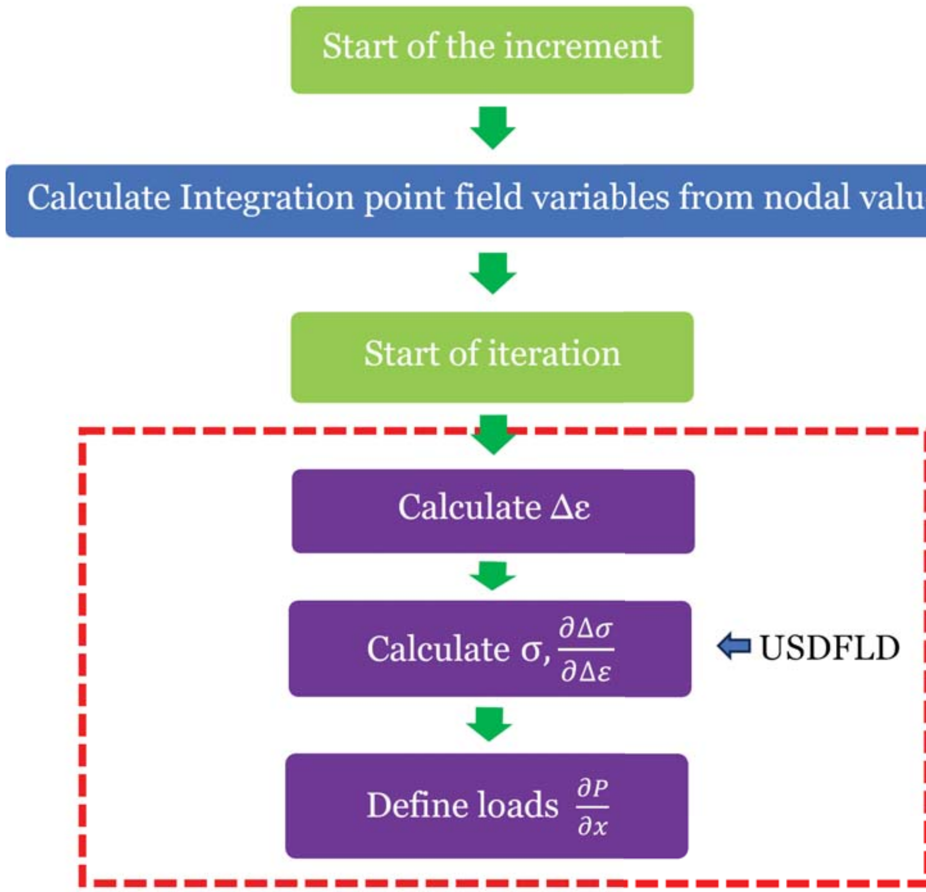

Fig. 4.6: Submission of USDFLD subroutine inside the time increment

the simulation can use a higher increment size initially and may increase the time increment if the solution converges in current iteration. In the same manner as linear analysis, displacements and rotations of each dummy node and corresponding forces and moments of reference nodes were extracted at the end of each increment using node output request.

4.4 Constitutive model

As discussed above, even without incorporating material non-linearity, a complex material model should be used in modelling homogenized composite tows to achieve a higher degree of accuracy. But if both geometric and material non-linearity needed to be incorporated in the analysis, a more sophisticated model will be required to handle localisation depend on the details of constitutive behaviour that are usually ignored because of their complexity.

Even if the observed strains in ultra thin composites are higher compared to the deformations that can be observed in thick woven composites, those can be still considered in the small strain range defined in abaqus (<5 %). Therefore, constitutive laws used in defining transversely isotropic material is valid for simulations in both linear and non-linear regime.

In this case, since the material behaviour introduced to ABAQUS using engineering constants, when simulation is carried out taking account geometrical non-linearity, Abaqus, the software will internally convert these engineering constants into the appropriate material model parameters for the specified constitutive model to accommodate large strains. In this case, hyper-elastic constitutive model based on strain energy potential will be defined compatible with the input parameters used for transversely isotropic material. General polynomial form of the strain energy function defined is,

$$U = \sum_{i+j=1}^{N} C_{ij}(I_1 - 3)^i (I_2 - 3)^j + \sum_{i=1}^{N} \frac{1}{D_i}(J_{el} - 1)^{2i} \tag{4.33}$$

where U is the strain energy potential, J_{el} is the elastic volume ratio, I_1 and I_2 are measures of distortion in the material and C_{ij}, D_i are material parameters. Here, the first part of the model describe the elastic deformation response of the material and the second part will impose a penalty to induce incompressibility of the material. As mentioned earlier, six separate analysis that will be performed in this study will be subjected to a strain or curvature in one direction at a time while all other strains restraining at zero. This will induce a noise due to the Poisson's effect at the boundaries that will be smoothed by above mentioned incompressibility penalty through the finite element mesh. Since we are applying the principle of virtual energy for the whole model to calculate ABD matrix, final calculated values will be independent of that effect.

Furthermore, when it comes to the material non-linear analysis, material data are specified as a function of solution dependent variable such as strain. USDFLD subroutine will allow to define material parameters as a function of the material point quantities and material directions. This access is made independently at each "constitutive calculation point." These points are the numerical integration points in the elements. Thus, the constitutive routines are concerned only with a single calculation point. The element provides an estimate of the kinematic solution to the problem at the point under consideration. These kinematic data are passed to the constitutive routines as the deformation gradient or, more typically, as the strain and rotation increments. The constitutive routines obtain the state at the point under consideration at the start of the increment from the “material point data base”. USDFLD subroutine will be called at each material point throughout the analysis and material parameters will be updated over every iteration for every material point. from a numerical viewpoint the implementation of a constitutive model involves the integration of the state of the material at an integration point over a time increment during a non-linear analysis. It should be noted that the implementation of constitutive models in ABAQUS assumes that the material behaviour is entirely defined by local effects, so each spatial integration point can be treated independently. Since ABAQUS/Standard is most commonly used with implicit time integration, the implementation must also provide an accurate “material stiffness matrix” for use in forming the Jacobian of the non-linear equilibrium equations. As a result, updating the material definition independently at each material point will not affect the accuracy or the integrity of the model.

CHAPTER 5

RESULTS AND DISCUSSION

First, following the procedure outlined in section 4.2.3, six separate unit strain analysis were performed considering both geometrical and material linear behaviour (Figure 5.1) and calculated the ABD matrix for the geometrically linear region.

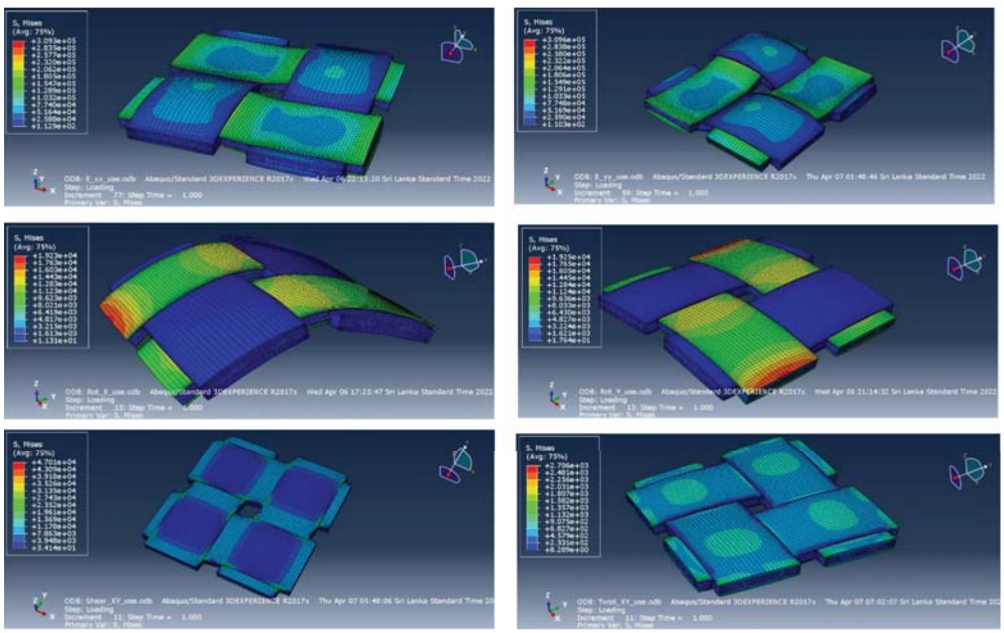

Fig. 5.1: Deformed configurations for analyses performed in linear region (a) Axial strain in X direction (b)Axial strain in Y direction (c)Rotation about X axis (d)Rotation about Y axis (e)Shear in XY plane (f)Twist

ABD stiffness matrix obtained for dry fibre model is presented below,

$$ABD_{Dryfibremodel} = \begin{pmatrix} 8493 & 2195 & 0 & | & 0 & 0 & 0 \\ 2195 & 8493 & 0 & | & 0 & 0 & 0 \\ 0 & 0 & 370 & | & 0 & 0 & 0 \\ -- & -- & -- & -- & -- & -- & -- \\ 0 & 0 & 0 & | & 36.5 & 4.7 & 0 \\ 0 & 0 & 0 & | & 4.7 & 36.5 & 0 \\ 0 & 0 & 0 & | & 0 & 0 & 1.8 \end{pmatrix} \tag{5.1}$$

The observed initial bending stiffness of the considered woven fibre composite (37.84) closely matched the results obtained from geometrically linear numerical analysis, with a deviation of 3.54% (within 5%). This indicates that the geometrical and numerical idealisations employed in the numerical analysis are sufficient to accurately capture the initial bending stiffness of the composite and to use in further simulations to capture the bending behaviour at higher curvatures.

Following the validation of the geometry, two separate analyses were conducted within the geometrically non-linear regime, under the assumption of linear elastic material behavior. In one model, contact regions were defined using tie constraints, while in the other, cohesive constraints were applied at the same interfaces. The objective was to investigate the influence of cohesive behavior on the observed reduction in bending stiffness.

One of our main hypotheses was that the relative slipping of tows at the contact regions causes the observed reduction in bending stiffness. To model these interactions, we used surface-based cohesive contact. In summary, surface-based contact is typically used for efficient modelling of global contact interactions, while element-based contact is used for more detailed and accurate modelling of localized contact behaviour. The choice between the two approaches depends on the specific requirements of the analysis, such as the size of the contact area, the complexity of the contact behaviour, and the available computational resources. It may not capture local contact phenomena accurately but, this choice proved to be adequate in idealising and accurately capturing the behaviour of the composite, as evidenced by the close agreement between the numerical simulations and the experimental results. However, it is worth to mention that the mesh alignment and quality were also crucial factors for accurate results.

In accordance with the methodology outlined in Section 4.3.2, six independent geometrically non-linear simulations were performed for both tie constraint model and cohessive constraint model. In each simulation, RUC was subjected to either a maximum curvature of 0.2 mm^{-1} or a maximum axial strain of 0.2. The simulation outputs were subsequently extracted at uniformly spaced time intervals. Given that curvature was applied incrementally in a linear fashion, the curvature corresponding to each time step was determined via linear interpolation. Using the extracted data and Equation 2.11, the corresponding constitutive response at each curvature level was computed.

Finally, the bending moment per unit width was plotted as a function of the applied curvature over the course of the simulation (Figure 5.2).

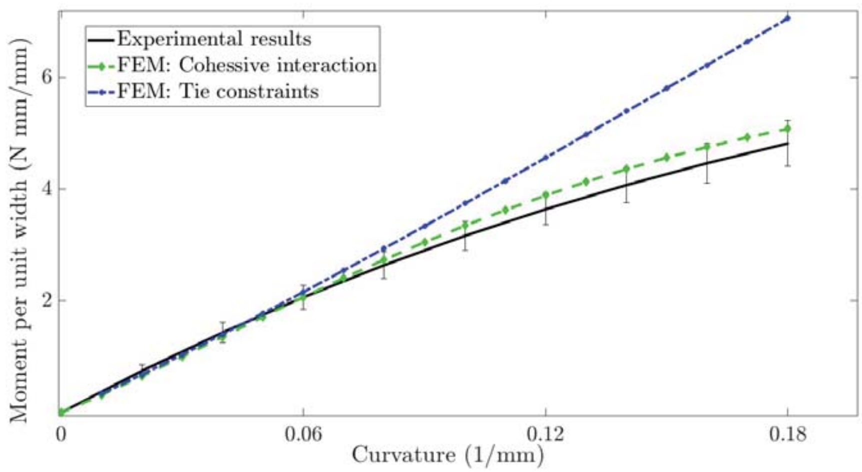

Fig. 5.2: Moment-curvature responses obtained from linear material models with experimental observations from [6]

The moment–curvature plot demonstrates that the finite element model employing tie constraints significantly overestimates bending stiffness at higher curvatures, exhibiting a stiffening response that deviates from the experimentally observed behavior. This discrepancy arises because tie constraints enforce perfect bonding between adjacent layers or components, preventing any relative displacement or delamination at the interfaces. As a result, the model unrealistically suppresses interfacial shear deformation and energy dissipation mechanisms that are typically present in real materials, especially under large curvatures. In contrast, cohesive constraints allow for progressive separation and sliding at the interfaces, more accurately replicating the physical behavior and leading to a bending response that better aligns with experimental observations. The inability of the tie constraint model to capture these interfacial effects results in an artificially increased stiffness and a failure to reflect the bending stiffness reduction observed in the experiments.

The numerically obtained bending behaviour, which initially accounted only for geometric non-linear effects, produced results that were closely aligned with the experimentally observed behaviour (Figure 5.2). This demonstrated the adequacy of the geometric non-linear model in capturing the essential bending characteristics of the material. However, another hypothesis was that material non-linearity affects the observed reduction in bending stiffness at higher curvatures. While the numerical results were reasonably close to the experimental observations even without incorporating material non-linearity, including it refined the simulations and brought the results into closer alignment with the experimental data. When dealing with non-linear materials, the internal forces are still governed by the stress-strain relationship of the material. However, this relationship may be non-linear, meaning that stress is not necessarily proportional to strain.

To apply the principle of virtual work with non-linear materials, we utilised incremental methods, which involve dividing the problem into small increments and assuming linear material behaviour within each increment. By applying the principle of virtual work incrementally for each step and updating stress and strain based on the material model, we were able to capture the complexities of material non-linearity accurately. FEA software, Abaqus, was used to implement these incremental methods, where it calculates internal forces based on the current deformation state and applies the principle of virtual work to determine the equilibrium configuration [9]. This approach ensured that our numerical simulations closely aligned with the experimental observations, confirming that our method for incorporating material non-linearity was correct and effective.

To achieve an even higher degree of accuracy and agreement with the experimental data, the analysis was further refined by incorporating the effects of material non-linearity as discussed in section 4.3. Both simulations were performed using the same geometrical and interface configurations, with the only difference being the material constitutive model assigned to tows. By including material non-linearities, the enhanced model provided a more comprehensive and precise representation of the bending behaviour (Figure 5.3). This refinement led to numerical predictions that closely matched the experimental observations, thereby validating the improved model and its ability to more accurately simulate the complex interactions affecting the bending performance of the material.

The plot (Figure 5.3) shows the comparison between experimental bending response (black solid line) and two numerical models of the composite laminate with cohesive constraints: one incorporating material non-linear behavior (magenta dashed line with stars), and the other assuming material linearity (dry-fibre model) (green dashed line with diamonds). This additional consideration of material non-linearity

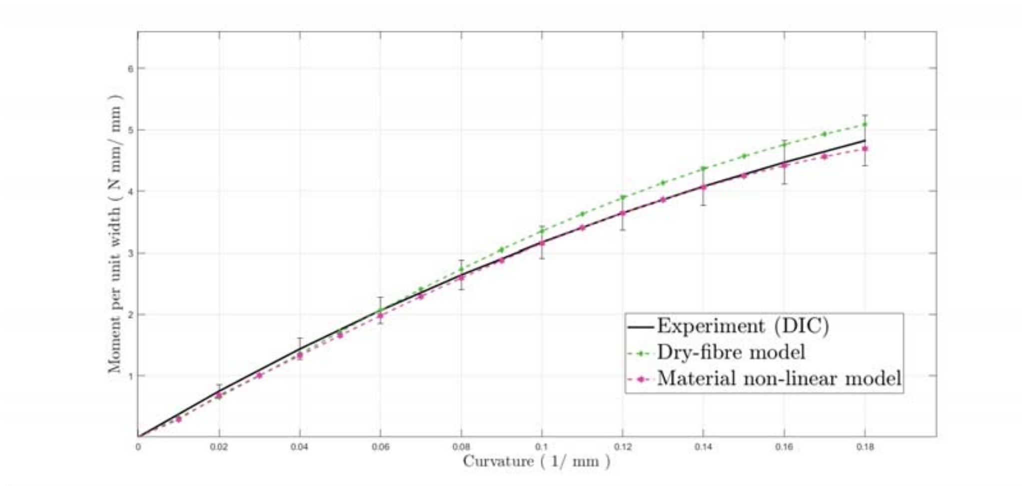

Fig. 5.3: Moment-curvature responses obtained from numerical models and experimental observations [6],[14]

enhanced the accuracy of the model, ensuring that the numerical predictions more precisely coincided with the observed experimental behaviour.

Both numerical models predict the initial bending stiffness reasonably well and remain within the experimental error bars throughout the deformation range. However, as the curvature increases, the response of the dry-fibre model begins to diverge from the experimental data, increasingly overestimating the bending moment. This discrepancy arises from the assumption of linear elastic behavior, which fails to capture the progressive stiffness degradation occurring in real composites due to mechanisms such as matrix micro-cracking, fibre-matrix interface debonding, and fibre reorientation. These damage processes are inherently non-linear and become more prominent at larger curvatures, where the material response deviates from the idealized elastic regime.

In contrast, the material non-linear model accounts for these effects by incorporating a strain-dependent reduction in stiffness and plasticity or damage evolution in the matrix-dominated directions. As a result, it provides a more accurate representation of the composite behavior over the entire deformation range, especially in the post-elastic region. This improved agreement with experimental data highlights the importance of using a material non-linear formulation when modeling composite structures subjected to large bending deformations. While both models may be suitable for small-deformation predictions, the non-linear model is essential for reliably capturing the stiffness reduction and energy dissipation mechanisms that govern the true mechanical response under realistic loading conditions.

CHAPTER 6

CONCLUSION AND FUTURE WORKS

Our primary goal was to accurately capture the observed geometrical non-linear bending behavior of ultra-thin woven composites. We hypothesized that the reduction in bending stiffness observed at higher curvatures could be effectively modeled by incorporating several key factors: the precise geometric architecture of the composites, the cohesive behavior at contact regions, the non-linear behavior of the material, and the geometric non-linear effects of bending.

To test this hypothesis, we performed detailed numerical simulations that included all these factors. The numerical results were then compared with experimental observations to evaluate the accuracy of our model. The results showed a strong agreement between the numerical and experimental data, confirming that our hypothesis was correct. Specifically, the simulations were able to capture the bending behavior accurately up to a curvature value of 0.2 mm^{-1}.

This agreement indicates that the methods we used in simulating these scenarios were robust and sufficient for capturing the complex bending behavior of ultra-thin woven composites. The success of our approach demonstrates the importance of considering multiple interacting factors, such as geometric and material non-linearities, to achieve a realistic and precise representation of the composite's behavior under bending stresses.

Although our study has successfully captured the observed bending behavior of ultra-thin woven composites, further research is needed to deepen our understanding of the underlying mechanisms. A comprehensive parametric analysis should be conducted to systematically evaluate and quantify which specific geometrical mechanisms are responsible for the reduction in bending stiffness and to assess their relative contributions. This will provide detailed insights into how different geometric factors interact and influence the material's performance.

Additionally, it is essential to simulate the failure mechanisms of these composites, especially given their application in structures subjected to extreme curvatures. Understanding how and when these composites fail under high curvature conditions will be crucial for developing design guidelines and improving the reliability and safety of future structures. By incorporating both the parametric analysis and failure simulations into future work, we can enhance our knowledge of composite behavior, refine design approaches, and ensure that these materials perform optimally in practical applications.

REFERENCES

[1] D. Adams and M. Mobrem, *MARSIS Antenna Flight Deployment Anomaly and Resolution*. [Online]. Available: https://arc.aiaa.org/doi/abs/10.2514/6.2006-1684

[2] S. Lomov, G. Huysmans, Y. Luo, R. Parnas, A. Prodromou, I. Verpoest, and F. Phelan, "Textile composites: modelling strategies," *Composites Part A: Applied Science and Manufacturing*, vol. 32, no. 10, pp. 1379–1394, 2001. [Online]. Available: https://www.sciencedirect.com/science/article/pii/S1359835X01000380

[3] Soykasap, "Analysis of tape spring hinges," *International Journal of Mechanical Sciences - INT J MECH SCI*, vol. 49, pp. 853–860, 09 2007.

[4] H. Mallikarachchi, "Predicting mechanical properties of thin woven carbon fiber reinforced laminates," *Thin-Walled Structures*, vol. 135, pp. 297–305, 2019. [Online]. Available: https://www.sciencedirect.com/science/article/pii/S0263823118308887

[5] A. Sharma, T. Rose, A. Seamone, T. Murphey, and F. Lopez Jimenez, "Analysis of the column bending test for large curvature bending of high strain composites," 01 2019.

[6] E. Gamage, U. Weerasinghe, H. Wijesooriya, S. Herath, and C. Mallikarachchi, "Non-linear bending response of ultra-thin woven fibre composites at large curvatures," *International Journal of Mechanical Sciences*, 2024 under review.

[7] R. Jones, *Mechanics of Composite Materials*, ser. International student edition. Scripta Book Company, 1975. [Online]. Available: https://books.google.com/books?id=lzXT3ANLrBgC

[8] S. Herath, M. Jayasekara, and C. Mallikarachchi, "Parametric study on the homogenized response of woven carbon fibre composites," 07 2020.

[9] M. Smith, *ABAQUS/Standard User's Manual, Version 6.9*. United States: Dassault Systèmes Simulia Corp, 2009.

[10] A. García-Carpintero, B. van den Beuken, S. Haldar, M. Herráez, C. González, and C. Lopes, “Fracture behaviour of triaxial braided composites and its simulation using a multi-material shell modelling approach,” *Engineering Fracture Mechanics*, vol. 188, pp. 268–286, 2018. [Online]. Available: https://www.sciencedirect.com/science/article/pii/S0013794417302576

[11] Mojtaba Komeili, “Mechanical behaviour of woven fabric composites under meso level uncertainities : Modeling and sensitivity analysis,” no. August, 2010.

[12] M. Sakovsky, S. Pellegrino, and H. Mallikarachchi, *Folding and Deployment of Closed Cross-Section Dual-Matrix Composite Booms*. [Online]. Available: https://arc.aiaa.org/doi/abs/10.2514/6.2016-0970

[13] D. M. S. P. Dassanayake, S. Navaratnarajah, and C. Mallikarachchi, “Quasi-static deployment simulation of a kapton polyimide creased unit,” in *2022 Moratuwa Engineering Research Conference (MERCon)*, 2022, pp. 1–6.

[14] C. Mallikarachchi and S. Pellegrino, “Deployment dynamics of ultrathin composite booms with tape-spring hinges,” *Journal of Spacecraft and Rockets*, vol. 51, 02 2014.

[15] J. Block, M. Straubel, and M. Wiedemann, “Ultralight deployable booms for solar sails and other large gossamer structures in space,” vol. 68, 04 2011.

[16] C. Leclerc and S. Pellegrino, “Nonlinear elastic buckling of ultra-thin coilable booms,” *International Journal of Solids and Structures*, vol. 203, 07 2020.

[17] G. Sanford, A. Biskner, and T. Murphey, “Large strain behavior of thin unidirectional composite flexures,” in *51st AIAA/ASME/ASCE/AHS/ASC Structures, Structural Dynamics, and Materials Conference*, 2010.

[18] J. M. Fernandez and T. W. Murphey, *A Simple Test Method for Large Deformation Bending of Thin High Strain Composite Flexures*. [Online]. Available: https://arc.aiaa.org/doi/abs/10.2514/6.2018-0942

[19] C. Bris and T. Lelièvre, “Multiscale modelling of complex fluids: A mathematical initiation,” *Lecture Notes in Computational Science and Engineering*, vol. 66, 01 2009.

[20] W. R. Smith and G. B. Wilkes, “Thermal conductivity of carbon blacks,” *Industrial & Engineering Chemistry*, vol. 36, no. 12, pp. 1111–1112, 1944. [Online]. Available: https://doi.org/10.1021/ie50420a007

[21] T. Gu, J. R. Medy, V. Fabien, O. Castelnau, S. Forest, E. Hervé-Luanco, F. Lecouturier-Dupouy, H. Proudhon, P.-O. Renault, and L. Thilly, “Multiscale modeling of the anisotropic electrical conductivity of architectured and nanostructured cu-nb composite wires and experimental comparison,” *Acta Materialia*, vol. 141, 09 2017.

[22] K. S. Campbell, B. S. Chrisman, and S. G. Campbell, “Multiscale modeling of cardiovascular function predicts that the end-systolic pressure volume relationship can be targeted via multiple therapeutic strategies,” *Frontiers in Physiology*, vol. 11, 2020. [Online]. Available: https://www.frontiersin.org/articles/10.3389/fphys.2020.01043

[23] T. Ishikawa and T.-W. Chou, “Elastic behavior of woven hybrid composites,” *Journal of Composite Materials*, Jul. 2016.

[24] S. Song, A. M. Waas, K. W. Shahwan, O. Faruque, and X. Xiao, “Compression response of 2d braided textile composites: Single cell and multiple cell micromechanics based strength predictions,” *Journal of Composite Materials*, vol. 42, no. 23, pp. 2461–2482, 2008. [Online]. Available: https://doi.org/10.1177/0021998308096500

[25] K.-H. Tsai, C.-L. Hwan, W.-L. Chen, and C.-H. Chiu, “A parallelogram spring model for predicting the effective elastic properties of 2d braided composites,” *Composite Structures*, vol. 83, no. 3, pp. 273–283, 2008. [Online]. Available: https://www.sciencedirect.com/science/article/pii/S0263822307001250

[26] D. Goyal, X. Tang, J. D. Whitcomb, and A. D. Kelkar, “Effect of various parameters on effective engineering properties of 2×2 braided composites,” *Mechanics of Advanced Materials and Structures*, vol. 12, no. 2, pp. 113–128, 2005.

[27] R. Karkkainen and B. Sankar, “A direct micromechanics method for analysis of failure initiation of plain weave textile composites,” *Composites Science and Technology*, vol. 66, pp. 137–150, 01 2006.

[28] X. Ji, A. M. Khatri, E. S. Chia, R. K. Cha, B. T. Yeo, S. C. Joshi, and Z. Chen, “Multi-scale simulation and finite-element-assisted computation of elastic properties of braided textile reinforced composites,” *Journal of Composite Materials*, vol. 48, no. 8, pp. 931–949, 2014. [Online]. Available: https://doi.org/10.1177/0021998313480198

[29] B. David and H. Patrice, “Stiffness and failure modelling of 2d and 3d textile-reinforced composites by means of imbricate-type elements approaches,” *Computers Structures - COMPUT STRUCT*, vol. 80, pp. 2253–2264, 11 2002.

[30] P. Tan, L. Tong, and G. P. Steven, “Modeling approaches for 3d orthogonal woven composites,” *Journal of Reinforced Plastics and Composites*, vol. 17, no. 6, pp. 545–577, 1998. [Online]. Available: https://doi.org/10.1177/073168449801700605

[31] A. Tabiei and Y. Jiang, “Woven fabric composite material model with material nonlinearity for nonlinear finite element simulation,” *International Journal of Solids and Structures*, vol. 36, no. 18, pp. 2757–2771, 1999. [Online]. Available: https://www.sciencedirect.com/science/article/pii/S0020768398001279

[32] A. Gasser, P. Boisse, and S. Hanklar, “Mechanical behaviour of dry fabric reinforcements. 3d simulations versus biaxial tests,” *Computational Materials Science*, vol. 17, no. 1, pp. 7–20, 2000. [Online]. Available: https://www.sciencedirect.com/science/article/pii/S0927025699000865

[33] G. Hivet, E. Vidal-Sallé, and P. Boisse, “Analysis of the stress components in a textile composite reinforcement,” *Journal of Composite Materials*, vol. 47, no. 3, pp. 269–285, 2013. [Online]. Available: https://doi.org/10.1177/0021998312439222

[34] D. Ballhause, M. König, and B. Kröplin, “Modelling of woven fabrics with the discrete element method,” *Cmc-computers Materials & Continua*, vol. 4, pp. 507–507, 2006. [Online]. Available: https://api.semanticscholar.org/CorpusID:134201070

[35] G. Hivet and P. Boisse, “Consistent mesoscopic mechanical behaviour model for woven composite reinforcements in biaxial tension,” *Composites Part*

B: Engineering, vol. 39, no. 2, pp. 345–361, 2008. [Online]. Available: https://www.sciencedirect.com/science/article/pii/S1359836807000297

[36] R. L. Karkkainen and B. V. Sankar, "A direct micromechanics method for analysis of failure initiation of plain weave textile composites," *Composites Science and Technology*, vol. 66, no. 1, pp. 137–150, 2006. [Online]. Available: https://www.sciencedirect.com/science/article/pii/S0266353805001910

[37] A. Kueh and S. Pellegrino, "Triaxial weave fabric composites," 01 2007.

[38] H. S. Wijesuriya, "Predicting non-linear bending behaviour of ultra-thin woven fibre composites," Ph.D. dissertation, 2019.

[39] S. Green, A. Long, B. El Said, and S. Hallett, "Numerical modelling of 3d woven preform deformations," *Composite Structures*, vol. 108, pp. 747–756, 2014. [Online]. Available: https://www.sciencedirect.com/science/article/pii/S026382231300528X

[40] R. A. Naik, P. G. Ifju, and J. E. Masters, "Effect of fiber architecture parameters on deformation fields and elastic moduli of 2-d braided composites," *Journal of Composite Materials*, vol. 28, pp. 656 – 681, 1994. [Online]. Available: https://api.semanticscholar.org/CorpusID:135635636

[41] S. Lomov, *WiseTex—A Virtual Textile Composites Software*. Cham: Springer International Publishing, 2022, pp. 293–318. [Online]. Available: https://doi.org/10.1007/978-3-030-91515-5_7

[42] L. Brown and A. Long, "8 - modeling the geometry of textile reinforcements for composites: Texgen," in *Composite Reinforcements for Optimum Performance (Second Edition)*, second edition ed., ser. Woodhead Publishing Series in Composites Science and Engineering, P. Boisse, Ed. Woodhead Publishing, 2021, pp. 237–265. [Online]. Available: https://www.sciencedirect.com/science/article/pii/B9780128190050000083

[43] N. Gowrikanthan, M. Jayasekara, C. Mallikarachchi, and S. Herath, "Effects of tow arrangements on the homogenized response of carbon fiber woven composites," *Composite Structures*, vol. 300, p. 116081,

2022. [Online]. Available: https://www.sciencedirect.com/science/article/pii/S0263822322008200

[44] L. Brown, mike matveev, and georgespackman, "louisepb/texgen: Texgen v3.13.0," Jul. 2023. [Online]. Available: https://doi.org/10.5281/zenodo.8189683

[45] S. Herath, M. Jayasekara, and C. Mallikarachchi, "Parametric study on the homogenized response of woven carbon fibre composites," in *2020 Moratuwa Engineering Research Conference (MERCon)*, 2020, pp. 36–41.

[46] S. Song, A. M. Waas, K. W. Shahwan, O. Faruque, and X. Xiao, "Compression response of 2d braided textile composites: Single cell and multiple cell micromechanics based strength predictions," *Journal of Composite Materials*, vol. 42, no. 23, pp. 2461–2482, 2008. [Online]. Available: https://doi.org/10.1177/0021998308096500

[47] J. Hughes, "Strength and modulus of current carbon fibres," *Carbon*, vol. 24, no. 5, pp. 551–556, 1986, proceedings of the Conference on Strength and Structural in Carbons and Graphites. [Online]. Available: https://www.sciencedirect.com/science/article/pii/0008622386901442

[48] V. Keryvin, A. Marchandise, and J.-C. Grandidier, "Non-linear elastic longitudinal behaviour of continuous carbon fibres/epoxy matrix composite laminae: Material or geometrical feature?" *Composites Part B: Engineering*, vol. 247, p. 110329, 2022. [Online]. Available: https://www.sciencedirect.com/science/article/pii/S1359836822007028

[49] G. Greaves, A. Greer, R. Lakes, and T. Rouxel, "Poisson's ratio and modern materials," *Nature materials*, vol. 10, p. 986, 11 2011.

[50] T. W. Murphey, G. E. Sanford, and M. M. Grigoriev, "Nonlinear elastic constitutive modeling of large strains in thin carbon fiber composite flexures," in *16th International conference on composite structures, Porto, Portugal*, 2011.

Appendix 01 – Python code utilized in modelling geometry.

```
#********************************************************************************
********************
# Test periodic BC
#********************************************************************************
********************
from abaqus import *
from abaqusConstants import *
import regionToolset
from part import *
from material import *
from section import *
from assembly import *
from step import *
from interaction import *
from load import *
from mesh import *
from optimization import *
from job import *
from sketch import *
from visualization import *
import connectorBehavior
from odbAccess import *
import math
import numpy as np
from numpy import mean, fmax
import mesh
import os

# Model parameters
a = 2.68
b = 2.68
c = 0.205
meshSize = 0.05
eps = meshSize/5.0
maxtowheight = 0.059

towwidth = 1.0
towlength = a

Model= mdb.models['dryF0dboth3']

p = Model.parts['PART-1']
```

```
ra = Model.rootAssembly
ins = ra.instances['PART-1-1']

# Create equation constraints: Approach 1 - Input file
#------------------------------------------------------------------------
# Pick node of face Z = 0.06 -> Corresponds to the mid plane of the bottom ply
n = ins.nodes
face1 = n.getByBoundingBox(-(eps),-(eps),-eps + 0.05844, a + eps, b + eps,
0.05844 + eps ) # 0.05956

# Create text file

eqFile = open('periodicBC.dat','w+')
#eqFile.write("coordinates %s \n" % (face1))
#eqFile.write("max min coordinates (%.5f %.5f), (%.5f %.5f), (%.5f %.5f) \n" %
(numpy.fmax(xcoordVec)))
#eqFile.write("max min coordinates (%.5f  \n" % (numpy.fmax(xcoordVec)))

# RVE midpoint Z val = 117.44E-03

P1count = 1
Q1count = 1
R1count = 1
S1count = 1

RefNodesPR = 1

RefPoint_X = np.arange(54)
RefPoint_Y = np.arange(54)

# BOTTOM PLY
# Iterate over the nodes on the face1 of the twoply RVE. Here FACE1 refers to the
midplane of the BOTTOM ply
for II in range(len(face1)): # len(face1)
    # Coordinates of II-th node
    n1 = face1[II]
    coords = n1.coordinates
    x1 = coords[0]
    y1 = coords[1]
    z1 = coords[2]

    #eqFile.write("coordinates %.5f %.5f %.5f \n" % (x1,y1,z1))
    if z1 <= 0.05844 + 0.2*eps and z1 >= 0.05844 - 0.1*eps: # 0.05844 and 0.05956
        if y1 <= 0.0 + 0.2*eps or y1 >= 2.666 - 0.1*eps: # 0.00196, 2.66595
```

```
            eqFile.write("%d) x1, y1, z1 is (%.4f, %.4f, %.4f) \n" % (II,
x1,y1,z1))
            ra.ReferencePoint(point=(x1, y1, 117.44E-03))
            box1 = n.getByBoundingBox(-1.0*(eps) + x1,-1.0*(eps) + y1,-eps -
maxtowheight/2. + z1, x1 + eps, y1 + eps, + 0.1*eps + maxtowheight/2. + z1 )

            if y1 < 0.1:
                # Create node set
                name1 = 'S_1_%d'% S1count
                ra.Set(name = name1, nodes = box1)
                RPn = (ra.referencePoints.findAt((x1, y1, 117.44E-03)),)
                refNodename = 'RP_S_1_%d'% S1count
                ra.Set(referencePoints=RPn, name = refNodename)

                #Create Dummy nodes
                ra.ReferencePoint(point=(x1, y1 - 0.2, 117.44E-03))
                RPn = (ra.referencePoints.findAt((x1, y1 - 0.2, 117.44E-03)),)
                refNodename = 'NODE_X%d'% S1count
                ra.Set(referencePoints=RPn, name = refNodename)

                # apply MPCs along vertical nodes on each tow boundary
                region1 = ra.sets['RP_S_1_%d'% S1count]
                region2 = ra.sets['S_1_%d'% S1count]
                Model.MultipointConstraint(name='MPC_S_1_%d'% S1count,
                controlPoint=region1, surface=region2, mpcType=BEAM_MPC,
                userMode=DOF_MODE_MPC, userType=0, csys=None)

                RefPoint_X[S1count-1] = x1

                S1count = S1count + 1

            elif y1 > 2.65:
                # Create node set
                name1 = 'Q_1_%d'% Q1count
                ra.Set(name = name1, nodes = box1)
                RPn = (ra.referencePoints.findAt((x1, y1, 117.44E-03)),)
                refNodename = 'RP_Q_1_%d'% Q1count
                ra.Set(referencePoints=RPn, name = refNodename)

                # apply MPCs
                region1 = ra.sets['RP_Q_1_%d'% Q1count]
                region2 = ra.sets['Q_1_%d'% Q1count]
                Model.MultipointConstraint(name='MPC_Q_1_%d'% Q1count,
                controlPoint=region1, surface=region2, mpcType=BEAM_MPC,
                userMode=DOF_MODE_MPC, userType=0, csys=None)
```

```
                Q1count = Q1count + 1

    if z1 <= 0.05844 + 0.2*eps and z1 >= 0.05844 - 0.1*eps: # 0.05844 and 0.05956
        if x1 <= 0.0 + 0.2*eps or x1 >= 2.666 - 0.1*eps: # 0.00196, 2.66595
            eqFile.write("%d) x1, y1, z1 is (%.4f, %.4f, %.4f) \n" % (II,
x1,y1,z1))

            # Create Reference nodes on P and R edges
            ra.ReferencePoint(point=(x1, y1, 117.44E-03))
            #refNode = ra.ReferencePoint(point=(x1, y1, 117.44E-03))
            box1 = n.getByBoundingBox(-1.0*(eps) + x1,-1.0*(eps) + y1,-eps -
maxtowheight/2. + z1, x1 + eps, y1 + eps, + 0.1*eps + maxtowheight/2. + z1 )

            if x1 < 0.1:
                # Create node set
                name1 = 'P_1_%d'% P1count
                ra.Set(name = name1, nodes = box1)
                RPn = (ra.referencePoints.findAt((x1, y1, 117.44E-03)),)
                refNodename = 'RP_P_1_%d'% P1count
                ra.Set(referencePoints=RPn, name = refNodename)

                #Create Dummy nodes
                ra.ReferencePoint(point=(x1 - 0.2, y1, 117.44E-03))
                RPn = (ra.referencePoints.findAt((x1 - 0.2, y1, 117.44E-03)),)
                refNodename = 'NODE_Y%d'% P1count
                ra.Set(referencePoints=RPn, name = refNodename)

                # apply MPCs
                region1 = ra.sets['RP_P_1_%d'% P1count]
                region2 = ra.sets['P_1_%d'% P1count]
                Model.MultipointConstraint(name='MPC_P_1_%d'% P1count,
                controlPoint=region1, surface=region2, mpcType=BEAM_MPC,
                userMode=DOF_MODE_MPC, userType=0, csys=None)

                RefPoint_Y[P1count-1] = y1

                P1count = P1count + 1

            elif x1 > 2.65:
                # Create node set
                name1 = 'R_1_%d'% R1count
                ra.Set(name = name1, nodes = box1)
                RPn = (ra.referencePoints.findAt((x1, y1, 117.44E-03)),)
                refNodename = 'RP_R_1_%d'% R1count
```

```
                ra.Set(referencePoints=RPn, name = refNodename)

                # apply MPCs
                region1 = ra.sets['RP_R_1_%d'% R1count]
                region2 = ra.sets['R_1_%d'% R1count]
                Model.MultipointConstraint(name='MPC_R_1_%d'% R1count,
                controlPoint=region1, surface=region2, mpcType=BEAM_MPC,
                userMode=DOF_MODE_MPC, userType=0, csys=None)

                R1count = R1count + 1

    # Pick pair of nodes on the opposite faces
    node1 = n.getByBoundingSphere((0.9249,2.666,0.05844), eps )
    node2 = n.getByBoundingSphere((x1,1.96E-03,0.05844), eps )
    #eqFile.write("coordinates %.5f %.5f %.5f and lengths are : %i %i \n" %
(x1,y1,z1,len(node1),len(node2)))

# TOP PLY
# Reference points are as same as the BOTTOM PLY because there is no phase
difference. So no need to have RP_i_'2' s for topply eg line 200
P2count = 1
Q2count = 1
R2count = 1
S2count = 1

face2 = n.getByBoundingBox(-(eps),-(eps),-eps + 176.44E-03, a + eps, b + eps,
176.44E-03 + eps ) # 0.05956

# Iterate over the nodes on the face2 of the twoply RVE. Here FACE2 refers to the
midplane of the TOP ply
for II in range(len(face2)): # len(face2)
    # Coordinates of II-th node
    n1 = face2[II]
    coords = n1.coordinates
    x1 = coords[0]
    y1 = coords[1]
    z1 = coords[2]

    #eqFile.write("coordinates %.5f %.5f %.5f \n" % (x1,y1,z1))
    if z1 <= 176.44E-03 + 0.2*eps and z1 >= 176.44E-03 - 0.1*eps: # 0.05844 and
0.05956
        if y1 <= 0.0 + 0.2*eps or y1 >= 2.666 - 0.1*eps: # 0.00196, 2.66595
            eqFile.write("%d) x1, y1, z1 is (%.4f, %.4f, %.4f) \n" % (II,
x1,y1,z1))
            #ra.ReferencePoint(point=(x1, y1, 117.44E-03))
```

```
            box1 = n.getByBoundingBox(-1.0*(eps) + x1,-1.0*(eps) + y1,-eps -
maxtowheight/2. + z1, x1 + eps, y1 + eps, + 0.1*eps + maxtowheight/2. + z1 )

            if y1 < 0.1:
                # Create node set
                name1 = 'S_2_%d'% S2count
                ra.Set(name = name1, nodes = box1)
                RPn = (ra.referencePoints.findAt((x1, y1, 117.44E-03)),)
                #refNodename = 'RP_S_2_%d'% S2count
                #ra.Set(referencePoints=RPn, name = refNodename)

                # apply MPCs
                region1 = ra.sets['RP_S_1_%d'% S2count]
                region2 = ra.sets['S_2_%d'% S2count]
                Model.MultipointConstraint(name='MPC_S_2_%d'% S2count,
                controlPoint=region1, surface=region2, mpcType=BEAM_MPC,
                userMode=DOF_MODE_MPC, userType=0, csys=None)

                S2count = S2count + 1

            elif y1 > 2.65:
                # Create node set
                name1 = 'Q_2_%d'% Q2count
                ra.Set(name = name1, nodes = box1)
                RPn = (ra.referencePoints.findAt((x1, y1, 117.44E-03)),)
                #refNodename = 'RP_Q_2_%d'% Q2count
                #ra.Set(referencePoints=RPn, name = refNodename)

                # apply MPCs
                region1 = ra.sets['RP_Q_1_%d'% Q2count]
                region2 = ra.sets['Q_2_%d'% Q2count]
                Model.MultipointConstraint(name='MPC_Q_2_%d'% Q2count,
                controlPoint=region1, surface=region2, mpcType=BEAM_MPC,
                userMode=DOF_MODE_MPC, userType=0, csys=None)

                Q2count = Q2count + 1

    if z1 <= 176.44E-03 + 0.2*eps and z1 >= 176.44E-03 - 0.1*eps: # 176.44E-03
and 177.56E-03
        if x1 <= 0.0 + 0.2*eps or x1 >= 2.666 - 0.1*eps: # 0.00196, 2.66595
            eqFile.write("%d) x1, y1, z1 is (%.4f, %.4f, %.4f) \n" % (II,
x1,y1,z1))
            #ra.ReferencePoint(point=(x1, y1, 117.44E-03))
            box1 = n.getByBoundingBox(-1.0*(eps) + x1,-1.0*(eps) + y1,-eps -
maxtowheight/2. + z1, x1 + eps, y1 + eps, + 0.1*eps + maxtowheight/2. + z1 )
```

```
            if x1 < 0.1:
                # Create node set
                name1 = 'P_2_%d'% P2count
                ra.Set(name = name1, nodes = box1)
                RPn = (ra.referencePoints.findAt((x1, y1, 117.44E-03)),)
                #refNodename = 'RP_P_2_%d'% P2count
                #ra.Set(referencePoints=RPn, name = refNodename)

                # apply MPCs
                region1 = ra.sets['RP_P_1_%d'% P2count]
                region2 = ra.sets['P_2_%d'% P2count]
                Model.MultipointConstraint(name='MPC_P_2_%d'% P2count,
                controlPoint=region1, surface=region2, mpcType=BEAM_MPC,
                userMode=DOF_MODE_MPC, userType=0, csys=None)

                P2count = P2count + 1

            elif x1 > 2.65:
                # Create node set
                name1 = 'R_2_%d'% R2count
                ra.Set(name = name1, nodes = box1)
                RPn = (ra.referencePoints.findAt((x1, y1, 117.44E-03)),)
                #refNodename = 'RP_R_2_%d'% R2count
                #ra.Set(referencePoints=RPn, name = refNodename)

                # apply MPCs
                region1 = ra.sets['RP_R_1_%d'% R2count]
                region2 = ra.sets['R_2_%d'% R2count]
                Model.MultipointConstraint(name='MPC_R_2_%d'% R2count,
                controlPoint=region1, surface=region2, mpcType=BEAM_MPC,
                userMode=DOF_MODE_MPC, userType=0, csys=None)

                R2count = R2count + 1

for I in range(1,55):
    # apply Equations PBCS

    # BOTTOM PLY
    # DOF 6
    Model.Equation(name='EQdof6-SQ-1-%d'% I, terms=((1.0, 'RP_Q_1_%d'% I, 6), (-
1.0, 'RP_S_1_%d'% I, 6), (0.0, 'NODE_X%d'% I, 6)))
    Model.Equation(name='EQdof6-PR-1-%d'% I, terms=((1.0, 'RP_R_1_%d'% I, 6), (-
1.0, 'RP_P_1_%d'% I, 6), (0.0, 'NODE_Y%d'% I, 6)))
    # DOF 5
```

```
    Model.Equation(name='EQdof5-SQ-1-%d'% I, terms=((1.0, 'RP_Q_1_%d'% I, 5), (-
1.0, 'RP_S_1_%d'% I, 5), (-2.664, 'NODE_X%d'% I, 5)))
    Model.Equation(name='EQdof5-PR-1-%d'% I, terms=((1.0, 'RP_R_1_%d'% I, 5), (-
1.0, 'RP_P_1_%d'% I, 5), (-2.664, 'NODE_Y%d'% I, 5)))
    # DOF 4
    Model.Equation(name='EQdof4-SQ-1-%d'% I, terms=((1.0, 'RP_Q_1_%d'% I, 4), (-
1.0, 'RP_S_1_%d'% I, 4), (2.664, 'NODE_X%d'% I, 4)))
    Model.Equation(name='EQdof4-PR-1-%d'% I, terms=((1.0, 'RP_R_1_%d'% I, 4), (-
1.0, 'RP_P_1_%d'% I, 4), (2.664, 'NODE_Y%d'% I, 4)))
    # DOF 3
    Model.Equation(name='EQdof3-SQ-1-%d'% I, terms=((1.0, 'RP_Q_1_%d'% I, 3), (-
1.0, 'RP_S_1_%d'% I, 3), (2.664*(2.664-RefPoint_X[I-1]), 'NODE_X%d'% I, 3)))
    Model.Equation(name='EQdof3-PR-1-%d'% I, terms=((1.0, 'RP_R_1_%d'% I, 3), (-
1.0, 'RP_P_1_%d'% I, 3), (2.664*(2.664-RefPoint_Y[I-1]), 'NODE_Y%d'% I, 3)))
    # DOF 2
    Model.Equation(name='EQdof2-SQ-1-%d'% I, terms=((1.0, 'RP_Q_1_%d'% I, 2), (-
1.0, 'RP_S_1_%d'% I, 2), (-2.664, 'NODE_X%d'% I, 2)))
    Model.Equation(name='EQdof2-PR-1-%d'% I, terms=((1.0, 'RP_R_1_%d'% I, 2), (-
1.0, 'RP_P_1_%d'% I, 2), (-2.664, 'NODE_Y%d'% I, 2)))
    # DOF 1
    Model.Equation(name='EQdof1-SQ-1-%d'% I, terms=((1.0, 'RP_Q_1_%d'% I, 1), (-
1.0, 'RP_S_1_%d'% I, 1), (-2.664, 'NODE_X%d'% I, 1)))
    Model.Equation(name='EQdof1-PR-1-%d'% I, terms=((1.0, 'RP_R_1_%d'% I, 1), (-
1.0, 'RP_P_1_%d'% I, 1), (-2.664, 'NODE_Y%d'% I, 1)))

    # TOP PLY is also attached to the RVE midplane (Refpoints) due to the non-
existent phase difference. Therefore, when EQs are defined for
    # ... midplane RVE, they are distributed to both the plies.


# Pick pair of nodes on the opposite faces
node1 = n.getByBoundingSphere((0.9249,2.666,0.05844), eps )
node2 = n.getByBoundingSphere((x1,1.96E-03,0.05844), eps )
#eqFile.write("coordinates %.5f %.5f %.5f and lengths are : %i %i \n" %
(x1,y1,z1,len(node1),len(node2)))

"""
    if len(node2)==0:
        nid1 = node1[0].label
    else:
        # Create node set
        nid1 = node1[0].label
        nid2 = node2[0].label
        name1 = 'Node-%d'%(nid1)
        name2 = 'Node-%d'%(nid2)
```

```
        # Define equation: u1-u2 = 0
        #eqFile.write('2 \n') # Number of terms in the equation
        #eqFile.write('PART-1-1.%d, 1, 1., PART-1-1.%d, 1, -1. \n'%(nid1,
nid2))   # NodeID-1, DoF-1, Coeff-1, NodeID2,... Note cube is the name of the
instance
        # Define equation: v1-v2 =0
        #eqFile.write('2 \n') # Number of terms in the equation
        #eqFile.write('PART-1-1.%d, 2, 1., PART-1-1.%d, 2, -1. \n'%(nid1,
nid2))   # NodeID-1, DoF-1, Coeff-1, NodeID2,... Note cube is the name of the
instance

        if II==0:
            # Define reference nodes
            n1ref = nid1
            n2ref = nid2
                # Define equation: u1-u2 = 0
                #eqFile.write('2 \n') # Number of terms in the equation
                #eqFile.write('PART-1-1.%d, 1, 1., PART-1-1.%d, 1, -1. \n'%(nid1,
nid2))   # NodeID-1, DoF-1, Coeff-1, NodeID2,... Note cube is the name of the
instance
                # Define equation: v1-v2 =0
                #eqFile.write('2 \n') # Number of terms in the equation
                #eqFile.write('PART-1-1.%d, 2, 1., PART-1-1.%d, 2, -1. \n'%(nid1,
nid2))   # NodeID-1, DoF-1, Coeff-1, NodeID2,... Note cube is the name of the
instance
        else:
            # Define equation: W1-W2 = W1ref - W2ref
            eqFile.write('')
            #eqFile.write('** Constraint: Eqn-%d \n*EQUATION \n'%(II))
            #eqFile.write('2 \n') # Number of terms in the equation
            #eqFile.write('PART-1-1.%d, 3, 1. \nPART-1-1.%d, 3, -1. \n'%(nid1,
nid2))   # NodeID-1, DoF-1, Coeff-1, NodeID2,... Note cube is the name of the
instance

                # Define equation: u1-u2 = 0
                #eqFile.write('2 \n') # Number of terms in the equation
                #eqFile.write('PART-1-1.%d, 1, 1., PART-1-1.%d, 1, -1. \n'%(nid1,
nid2))   # NodeID-1, DoF-1, Coeff-1, NodeID2,... Note cube is the name of the
instance
                # Define equation: v1-v2 =0
                #eqFile.write('2 \n') # Number of terms in the equation
                #eqFile.write('PART-1-1.%d, 2, 1., PART-1-1.%d, 2, -1. \n'%(nid1,
nid2))   # NodeID-1, DoF-1, Coeff-1, NodeID2,... Note cube is the name of the
instance
```

```
"""

eqFile.close()


# nnn=face1[II]
# coor=nnn.coordinates
# coor
```